



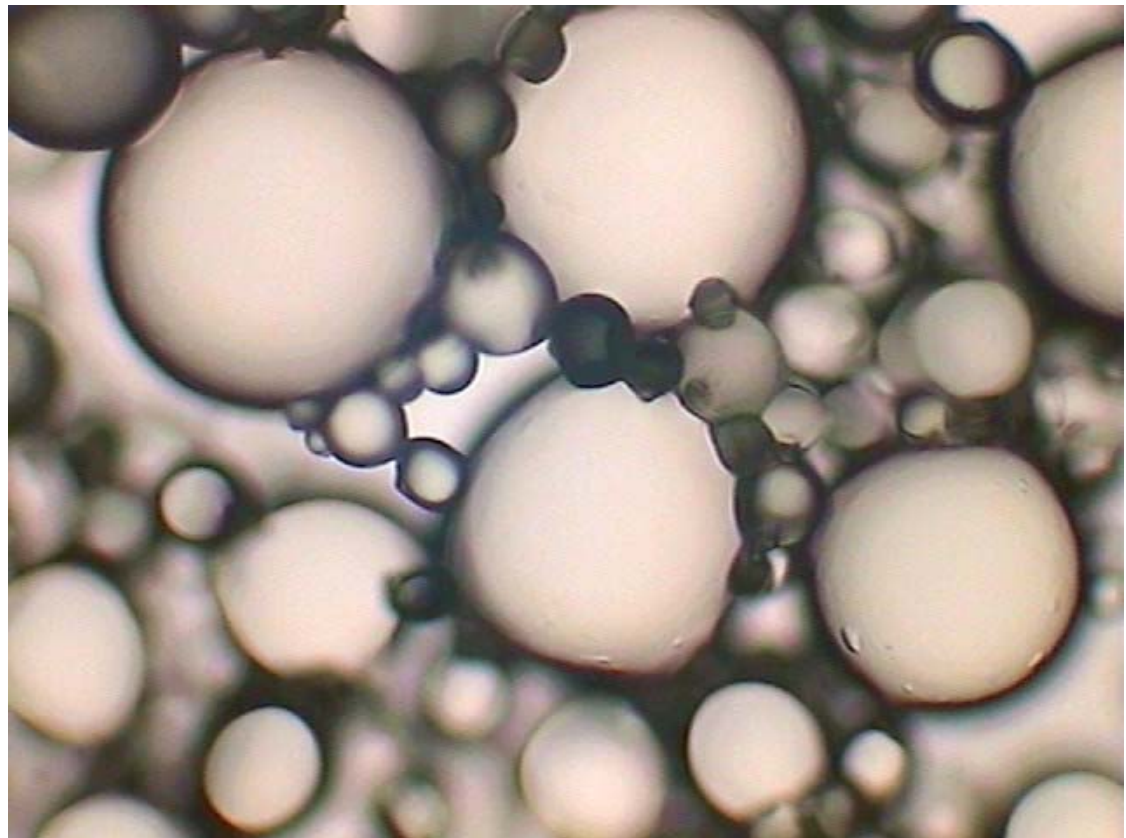
**US Army Corps
of Engineers®**
Engineer Research and
Development Center

Basic Research/Military Construction

Thermal Performance of Microencapsulated Phase Change Material Slurry

Jorge L. Alvarado, Barclay G. Jones, Charles P. Marsh,
David A. Kessler, Chang W. Sohn, Carl A. Feickert,
Gary E. Phetteplace, Eric D. Crowley, Ryan J. Franks, and
Thomas A. Carlson

March 2008



Thermal Performance of Microencapsulated Phase Change Material Slurry

Jorge L. Alvarado

*Department of Engineering Technology and Industrial Distribution
Texas A&M University
College Station, TX 77843-3367*

Charles P. Marsh, David A. Kessler, Chang W. Sohn, Carl A. Feickert, Eric D. Crowley,
Ryan J. Franks, and Thomas A. Carlson

*Construction Engineering Research Laboratory
U.S. Army Engineer Research and Development Center
2902 Newmark Drive
Champaign, IL 61822*

Gary E. Phetteplace

*Cold Regions Research and Engineering Laboratory
72 Lyme Road
Hanover, NH 03755-1290*

Barclay G. Jones

*Department of Nuclear, Plasma, and Radiological Engineering
University of Illinois, Urbana-Champaign
Urbana, IL 61801*

Final Report

Approved for public release; distribution is unlimited.

Prepared for U.S. Army Corps of Engineers
Washington, DC 20314-1000

Under Project 008BE4, Modeling of Heat-Transfer Fluids Containing Phase Change
Materials

Abstract: The efficiency of a pumped heat-transfer system can be greatly increased by incorporating a phase-change material (PCM). Because PCMs have greater thermal capacity than the carrier fluid, owing to their latent heat of phase change, they can increase the amount of heat transfer at equivalent volumetric flow in a heat exchanging environment. These materials tend to clog heat-transfer and distribution pipes, but previous research has indicated that the problem may be solved by encapsulating the PCMs. This report documents an investigation of the thermophysical properties of PCMs enclosed in micro-scale capsules. The study also addressed microcapsule durability against abrasion and chemicals, and the relation of fluid temperature and particle volume fraction on viscosity.

The results of this research show that the total heat capacity of microencapsulated PCM (MPCM) slurries is enhanced significantly, even when using low volume fractions. MPCM slurries have potential to decrease costs and improve energy efficiency for all pumped cooling applications.

DISCLAIMER: The contents of this report are not to be used for advertising, publication, or promotional purposes. Citation of trade names does not constitute an official endorsement or approval of the use of such commercial products. All product names and trademarks cited are the property of their respective owners. The findings of this report are not to be construed as an official Department of the Army position unless so designated by other authorized documents.

DESTROY THIS REPORT WHEN NO LONGER NEEDED. DO NOT RETURN IT TO THE ORIGINATOR.

Contents

Figures and Tables	v
Preface	vii
Unit Conversion Factors	viii
1 Introduction	9
Background	9
Objective	10
Approach.....	10
Mode of technology transfer.....	10
2 Thermophysical Aspects of Heat Transfer in Fluids	12
Properties of phase change materials	12
Particulate flow.....	13
<i>Heat transfer analysis</i>	13
<i>Effect of particles on fluid thermal conductivity</i>	15
Effects of microencapsulating PCMs	17
Enhanced pipe surfaces	21
3 MPCM Thermophysical Properties Characterization	22
Thermal properties determined by differential scanning calorimetry	22
<i>DSC apparatus and conditions</i>	23
<i>Experimental results</i>	25
<i>Latent heat of fusion</i>	25
<i>Specific heat</i>	26
<i>Melting and crystallization points</i>	27
<i>Nucleation issues</i>	28
<i>Chemical compatibility of capsule and anti-freezing additives</i>	31
Viscosity measurements	32
Durability testing	36
4 Heat Transfer Characterization of MPCM Slurry	38
Experimental system design.....	38
<i>Heat transfer section</i>	38
<i>Water pressure drop test</i>	40
<i>MPCM slurry pressure drop test</i>	41
<i>Convective heat transfer coefficient measurement for water</i>	45
MPCM slurry heat transfer test	46
5 Computational Modeling	57
Overview	57
Fundamental assumptions	57

Implementation	61
Results	65
6 Conclusion and Recommendations	72
Conclusions	72
Recommendations	73
References.....	74
Appendix: Effects of Temperature and Volume Fraction on Slurry Viscosity	77
Report Documentation Page.....	84

Figures and Tables

Figures

2.1	Scanning electron micrograph of typical MPCM in water carrier fluid.....	18
2.2	Detailed view of MPCMs at 100x magnification.....	18
3.1	Representative DSC endotherm curve.....	23
3.2	Latent heat of fusion of MPCM slurry (90 – 150 μm).....	26
3.3	Specific heat of MPCM slurry (90 – 150 μm).....	27
3.4	Melting and initiation of freezing points of MPCM slurry (90 – 150 μm).....	28
3.5	Degree of supercooling as a function of tetradecanol in tetradecane.....	29
3.6	Melting and freezing points of microencapsulated n-tetradecane with 2% tetradecanol (70 – 260 μm).....	29
3.7	Thermal cycling of MPCM with 2% tetradecanol.....	30
3.8	Methanol/water mixture viscosity as a function of concentration (lower concentration regions disallowed for freezing).....	32
3.9	MPCMs after 10 days in methanol mixture (20%), 100x magnification.....	32
3.10	Apparent viscosity of MPCM slurry as function of mass fraction and temperature (5 – 20 μm).....	34
3.11	Relative viscosity of MPCM slurry as function of mass fraction and temperature (5 – 20 μm).....	35
3.12	Schematic representation of durability loop.....	36
4.1	Schematic of heat transfer loop.....	39
4.2	Pressure drop of water with 8 mm enhanced tubing.....	41
4.3	Pressure drop of MPCM slurry at 5.9% mass fraction, 10.9 mm regular tubing.....	42
4.4	Pressure drop of MPCM slurry at 5.9% mass fraction, 8 mm regular and 8 mm enhanced tubing.....	43
4.5	Pressure drop of MPCM slurry at 13.4% and 15.2% mass fraction, 10.9 mm smooth tubing.....	44
4.6	Pressure drop of MPCM slurry at 13.4% and 15.2% mass fraction, 8 mm smooth, and 8 mm enhanced tubing.....	44
4.7	Temperature profile for MPCM slurry at 7.0%, 10.9 mm smooth tubing, Reynolds number range 3200 – 5400.....	48
4.8	Temperature profile for MPCM slurry at 7.0%, 10.9 mm smooth tubing, Reynolds number range 5800 – 7500.....	48
4.9	Heat transfer coefficient of MPCM slurry at 7.0%, 10.9 mm regular tubing, Reynolds number range 3200 – 5400.....	49
4.10	Heat transfer coefficient of MPCM slurry at 7.0%, 10.9 mm regular tubing, Reynolds number range 5800 – 7500.....	50
4.11	Temperature profile for MPCM slurry at 16.5%, 10.9 mm smooth tubing, Reynolds number ~ 4000.....	51

4.12	Heat transfer coefficient of MPCM slurry at 16.5%, 10.9 mm smooth tubing, Reynolds number ~ 4000.....	51
4.13	Heat transfer coefficient of MPCM slurry at 7.0%, 8 mm regular and 8 mm enhanced tubing at 1.9 m/sec, Reynolds number ~ 6900	52
4.14	Heat transfer coefficient of MPCM slurry at 12.0%, 8 mm regular tubing at 1.9 and 2.24 m/sec, equivalent Reynolds number range 4600 - 5400.....	53
4.15	Heat transfer coefficient of MPCM slurry at 6.5%, 8 mm enhanced tubing, equivalent Reynolds number range 6300 - 8900	54
4.16	Heat transfer coefficient of MPCM slurry at 15.2%, 8 mm enhanced tubing, Equivalent Reynolds number range 3900 - 4500	54
5.1	A typical mean velocity profile for turbulent pipe flow = 1.5 m/s.....	59
5.2	Two dimensional slices of melting region for (a) present model and (b) Choi et al (1999).....	60
5.3	Model geometry and boundary conditions (not drawn to scale).....	63
5.4	Computed and experimental (Yamagishi et al. 1999) bulk temperature profiles along pipe axis; $\ddot{q} = 19.984 \text{ kW/m}^2$, $\bar{u} = 1.25 \text{ m/s}$, and $\alpha = 0.12$	66
5.5	Computed and experimental (Alvarado 2004) bulk temperature profiles along pipe axis; $\ddot{q} = 18.3 \text{ kW/m}^2$, $\bar{u} = 1.50 \text{ m/s}$, and $\alpha = 0.07$	67
5.6	Computed and experimental (Alvarado 2004) bulk temperature profiles along pipe axis; $\ddot{q} = 8.3 \text{ kW/m}^2$, $\bar{u} = 0.83 \text{ m/s}$, and $\alpha = 0.07$	68
5.7	Computed and experimental (Alvarado 2004) heat transfer coefficient profiles along length of heat exchanger; $\ddot{q} = 18.3 \text{ kW/m}^2$, $\bar{u} = 1.50 \text{ m/s}$, and $\alpha = 0.07$	70
5.8	Computed and experimental (Alvarado 2004) heat transfer coefficient profiles along length of heat exchanger; $\ddot{q} = 8.3 \text{ kW/m}^2$, $\bar{u} = 0.92 \text{ m/s}$, and $\alpha = 0.07$	70
5.9	Computed and experimental (Yamagishi et al. 1999) heat transfer coefficient profiles along length of heat exchanger; $\ddot{q} = 19.984 \text{ kW/m}^2$, $\bar{u} = 1.25 \text{ m/s}$, and $\alpha = 0.07$	71

Tables

3.1	Thermal properties of MPCM based on DSC results.....	25
3.2	DSC results for third and four MPCM batches (5 - 20 μm)	30
3.3	Various compounds used as anti-freeze agents.....	31
3.4	Experimental conditions for durability tests	37
3.5	Results from durability experiments	37
4.1	Summary of percentage of particles migrating in and out of the near-wall region	55

Preface

This study was conducted for Headquarters, U.S. Army Corps of Engineers, under Research, Development, Test, and Evaluation (RDTE) Program AT23, “Basic Research/Military Construction”; Project 008BE4, “Modeling of Heat-Transfer Fluids Containing Phase Change Materials”. The technical monitor was Martin J. Savoie, CEERD-CV-T.

The work was performed by the Materials and Structures Branch (CF-M) of the Facilities Division (CF), Construction Engineering Research Laboratory (CERL), U.S. Army Engineer Research and Development Center (ERDC). The Project Manager was Dr. Charles P. Marsh. During the preparation of this report, Vicki L. Van Blaricum was Chief, CEERD-CF-M; L. Michael Golish was Chief, CEERD-CF; and Martin J. Savoie was the Technical Director for Installations. The Acting Deputy Director of ERDC-CERL was Dr. Kirankumar Topudurti, and the Director was Dr. Ilker Adiguzel.

The Commander and Executive Director of ERDC was COL Richard B. Jenkins and the Director was Dr. James R. Houston.

Unit Conversion Factors

Multiply	By	To Obtain
British thermal units (International Table)	1,055.056	joules
centipoises	0.001	pascals
cubic ft	0.02831685	cubic meters
cubic in.	1.6387064 E-05	cubic meters
degrees Fahrenheit	$(F-32)/1.8$	degrees Celsius
feet	0.3048	meters
gallons (U.S. liquid)	3.785412 E-03	cubic meters
inches	0.0254	meters
microns	1.0 E-06	meters
ounces (U.S. fluid)	2.957353 E-05	cubic meters
pounds (force)	4.448222	newtons
pounds (force) per square inch	6.894757	kilopascals

1 Introduction

Background

Phase change materials (PCM) have long been of interest as thermal storage and control media because of their large heat absorption and release capacity during a latent change in phase. Previous research has shown that PCMs can increase a fluid's heat transfer capacity by a factor of four (Yamagishi et al. 1999). Such an improvement would be highly desirable for applications such as district cooling and other applications of interest to the U.S. Army. Successful implementation of PCMs could increase operating efficiency (or decrease capital costs) of district cooling systems on military installations, and it also could decrease the size and weight of new cooling systems. Such improvements could position PCMs as an enabling technology to help lengthen military mission duration (e.g., improved micro-climate management for the warfighter), add mission capacity (e.g., greater materiel-carrying capacity in military vehicles), and improve fuel economy and logistics.

Although the potential benefits of PCMs in thermal transfer systems are considerable, a disadvantage of these materials is their tendency to clog distribution pipes. Some studies suggest that microencapsulating PCMs can reduce the undesirable properties of the materials while maintaining some of their unique beneficial properties (Winters 1991, cited in Yamagishi et al. 1999). By microencapsulating a PCM within a thin, durable polymer shell, the core material remains separated from the carrier fluid, thus preventing it from fouling the distribution system. The specific properties of microencapsulated PCMs (MPCMs) have not yet been investigated or characterized in great detail, however.

In order to advance the availability of MPCMs as an enabling technology for next-generation utility systems and military applications, the U.S. Army Engineer Research and Development Center, Construction Engineering Research Laboratory (ERDC-CERL) performed a series of experiments to investigate the fundamental thermodynamic, chemical, and mechanical factors affecting heat transfer and operational characteristics of MPCM slurries.

Objective

The objective of the study documented here was to characterize the thermal and fluid properties of MPCMs and MPCM slurries. The specific thermophysical properties of interest were:

- *latent heat of fusion* — the amount of **thermal energy** which must be absorbed or evolved for 1 **mole** of a substance to change states from a **solid** to a **liquid** or vice versa
- *apparent specific heat* — the measure of heat energy required to raise the temperature of one gram of a substance by one degree Celsius/Kelvin as determined experimentally
- *melting and crystallization temperature points* — the temperature at which a solid changes from liquid to solid or vice versa
- *apparent viscosity* — the measure of the resistance of a fluid to flow or deform as measured experimentally
- *heat transfer coefficient* — the collection of terms that denotes ease of heat transfer between a solid and moving fluid
- *pressure drop under turbulent conditions* — the change in force on a fluid resulting from non-laminar flow.

Approach

This work investigated many fundamental properties and engineering challenges associated with the use, development, and future application of MPCM slurries for enhanced heat transfer. Their thermal properties of latent heat of fusion and phase-change temperatures were experimentally determined using differential scanning calorimetry and other methods described in text. The effects of those properties on viscosity (including temperature dependence) and the associated pressure drop during pumped and entrained flow were also characterized. Various flow rates and values of heat flux were used. Initial measurements of microcapsule durability were also made. Concurrent modeling efforts encompassing fluid dynamics, phase change, and turbulent heat transfer were also undertaken to help understand the process.

Mode of technology transfer

Prospective future uses of this technology would include applications to decrease the size of cooling equipment and retrofits for existing equipment to significantly increase its cooling capacity. Such applications would require the update of applicable industry standards and Department of De-

fense criteria documents such as Unified Facilities Guide Specifications (UFGS) and Unified Facilities Criteria (UFC). Specifications for mobile engine applications could also be affected owing to the higher operating temperature and, thus, improved efficiency resulting from the greater capacity for heat removal.

2 Thermophysical Aspects of Heat Transfer in Fluids

Properties of phase change materials

PCM performance in heat exchange systems depends on factors such as the Stefan number, mass fraction, and the latent heat of fusion. In order for the PCM to be at optimal effectiveness, the Stefan number must be lower than 1 and defined as follows:

$$St = \frac{c_p \left(q_w \frac{R}{k} \right)}{c_m \lambda} \quad (2.1)$$

where:

C_p = suspension's specific heat

q_w = heat flux across the pipe wall

R = radius of pipe

k = suspension's thermal conductivity

C_m = mass fraction of PCM in suspension

λ = PCM's latent heat of fusion

High mass fractions and latent heat of fusion would intuitively be preferred because they permit a higher heat capacity. However, high mass fractions increase slurry viscosity, which in turn demands more pumping power.

Some researchers have added various paraffins in an attempt to match the PCM melting point to the optimal system temperature, but that approach also demands more pumping power, and it has proven to clog pipes in actual use (Chen and Chen 1987, Choi et al. 1991, Choi 1994, Dumas et al. 1994, He and Setterwall 2002, Kasza and Chen 1985). It was also found that melted PCM in the slurry tended to locate toward the surface of the heated tubing while the solid PCM remained more near to the core of the flow. Liquid paraffin was added to remedy that problem, but the thermal conductivity of liquid paraffin is lower than that of water, which limits the heat transfer and thus tends to negate the benefits of the PCM.

Particulate flow

Understanding of the nature of particulate flow is important to the investigation of a flowing system. The physics of particulate flow within slurry has been the topic of several pertinent studies. Before delving directly into particulate flow, however, general foundations of heat transfer analysis must be introduced.

Heat transfer analysis

The following text defines some intrinsic thermal properties of materials, and also some derived properties important to an understanding of heat transfer.

The *thermal conductivity* of a material is equivalent to the quantity of heat that passes in unit time through unit area of a plate when its opposite faces are subject to unit temperature gradient (1 degree temperature difference across a thickness of 1 unit):

$$\text{Thermal conductivity} = \text{heat flow rate}/(\text{area} \times \text{temperature gradient}) \quad (2.2)$$

It is measured in watts per meter-kelvin, $\text{W}\cdot\text{m}^{-1}\cdot\text{K}^{-1}$.

Heat capacity is the ability of a material to store heat:

$$\text{Heat capacity} = V * \rho * C_p \quad (2.3)$$

where:

$$\begin{aligned} V &= \text{volume (m}^3\text{)} \\ \rho &= \text{density (kg/m}^3\text{)} \\ C_p &= \text{specific heat (J/kg}\cdot\text{K)} \end{aligned}$$

It is measured in joules per kelvin (J/K).

Thermal diffusivity is the ratio of thermal conductivity to heat capacity. Substances with high thermal diffusivity will rapidly adjust their temperature to that of their surroundings, because they conduct heat quickly in comparison to their “thermal bulk.” This property is expressed as:

$$\alpha = \kappa/\rho C_p \quad (2.4)$$

where:

- α = thermal diffusivity
- κ = thermal conductivity
- ρ = density
- C_p = heat capacity

The units are m^2/s .

The *Prandtl number* is a dimensionless number that approximates the ratio of viscous diffusion rate to thermal diffusion rate, expressed as:

$$Pr = \nu/\alpha \quad (2.5)$$

where:

- Pr = Prandtl number
- ν = kinematic viscosity
- α = thermal diffusivity

The *Reynolds number* is perhaps the most important dimensionless number in fluid dynamics. It is used for determining whether a flow is laminar or turbulent. *Laminar flow* within pipes occurs when the Reynolds number is below the critical value of $Re_{crit, pipe} = 2300$; *turbulent flow* occurs when $Re_{crit, pipe} > 2300$, where the Reynolds number is based on the pipe diameter and the mean velocity v_s within the pipe. The value of 2300 has been determined experimentally, and an experiment-specific range around this value is considered the transition region between laminar and turbulent flow. The number is expressed as:

$$Re = vD/\nu \quad (2.6)$$

where:

- Re = Reynolds number
- v = velocity
- D = diameter of pipe
- ν = kinematic viscosity

The *Péclet number* is a dimensionless number relating the forced convection of a system to its heat conduction. It is equivalent to the product of the Reynolds number with the Prandtl number, as follows:

$$Pe = \frac{e * d^2}{\alpha} \quad (2.7)$$

where:

Pe = Peclet number

e = shear rate

d = particle diameter

a = heat diffusivity

Effect of particles on fluid thermal conductivity

Presence of particles

Ahuja (1975) showed that thermal conductivity could be increased by a factor of 2 in laminar conditions. Various researchers (Ahuja 1975, Collingham et al. 1970, Sohn and Chen 1981) discovered that particle rotation is one of the main mechanisms promoting greater heat transfer. Kasza and Chen (1985) observed that enhancement in heat transfer was poor for Peclet number less than 100. The results of those studies indicate that particles alone can increase thermal capacity of a fluid by microconvection in the laminar flow case, especially at high shear rates. Findings also suggest other mechanisms that increase thermal capacity, including particle migration and contributions from the latent heat of fusion of PCM. Sohn and Chen (1981) determined that for Peclet number higher than 300 the effective enhanced thermal conductivity approaches the power law $Pe^{1/2}$.

Effect of particle volume fraction on velocity profile

Changes in the volume fraction of particles in a fluid changes velocity profile and affects heat transfer. Fan et al. (1998) found that smaller particles match a fluid's velocity profile better than large ones in gas streams. Abbas and Crowe (1987) observed that 210 μm particles maintain a turbulent-like velocity profile. However, Chen and Kadambi (1994) found that at low Reynolds number and high volume fraction, slurry flow becomes heterogeneous and the velocity profile deviates from a single-phase fluid turbulent-like velocity profile. It was suggested that particle-to-particle, liquid-to-particle, and particle-to-wall interactions play a decisive role in conditioning the velocity profile. Experiments performed by Karnis et al. (1966) showed that as volume fraction of particles increased, partial plug flow developed and the particles traveling inside the central core did not rotate. Observations indicated that particles had irregular trajectories outside the core.

Effect of particle size and volume fraction on turbulence

Hetsroni (1993) suggests that particles can either suppress or promote turbulence depending on their size. A particle size between 5 to 10 wall units is recommended to enhance turbulence. A wall unit is defined as follows:

$$\text{Wall unit} = \frac{y \cdot u^*}{\nu} = \frac{d \cdot u^*}{\nu} \quad (2.8)$$

$$u^* = \sqrt{\frac{\tau}{\rho}} \quad (2.9)$$

u^* = friction velocity

d = particle size

ρ = fluid density

ν = fluid kinematic viscosity

τ = fluid shear stress

The fluid shear stress value can be obtained from pressure drop results. Rashidi et al. (1990) observed that particles of similar size but different densities did not differ in their ability to enhance turbulence. Tsuji et al. (1984) discovered that medium-size particles could reduce turbulence near the wall and increase it near the center. In those experiments, particles were larger than the Kolmogoroff scale,

$$\left(\frac{\nu^3}{\varepsilon} \right)^{1/4} \quad (2.10)$$

but about the same size as the Taylor scale,

$$\left(15\nu \frac{\overline{u'^2}}{\varepsilon} \right) \quad (2.11)$$

where ε is the viscous dissipation of turbulent energy $\overline{u'^2}$, and ν is kinematic viscosity.

Turbulence can also be suppressed as the volume fraction of particles increases because of higher apparent viscosity (Ahuja 1975). The term ap -

parent viscosity must be used because the material does not remain in a single phase through the complete cycle of this experiment.

Hetsroni (1989) and Fan et al. (1998) observed that when the particle Reynolds number (Re_p) is greater than 400, vortex shedding occurs resulting in turbulence enhancement. Also when Re_p is less than 100, no vortex shedding takes place and turbulence attenuation is observed.

Crowe et al. (1998) observed that the particle-diameter-to-fluid length scale (D_p/L_e) plays a decisive role in attenuating or enhancing turbulence. Crowe et al. (2000) observed turbulence enhancement for D_p/L_e greater than 0.1. Conversely, experimental data suggest that for D_p/L_e less than 0.1, turbulence was either suppressed or unchanged. Abbas and Crowe (1987) observed that liquid slurry made of particles in the 100 – 200 μm range, in turbulent flow and up to 20% volume fraction whose D_p/L_e was less than 0.001, exhibited small turbulence intensity, corroborating previous findings. In any case, particles smaller than 100 μm under similar circumstances will probably exhibit turbulence attenuation due to higher apparent viscosity and as predicted by D_p/L_e ratio. Gore and Crowe (1990) also observed that peaked turbulence intensity is shifted to higher Reynolds number when volume fraction increases. Experimental evidence also suggests that at higher particle volume fraction, inter-particle spacing is reduced, thus disrupting the turbulent eddies. Also, as slurries become denser, particle-to-particle interactions become more dominant.

Most researchers in the area of particulate flow have clearly identified specific characteristics of slurry or particulate flow – in particular the effect of particles and particle volume fraction on viscosity and turbulence. As a result, pipe geometry or flow conditions must be adjusted to compensate for suppressed turbulence.

Effects of microencapsulating PCMs

Figure 2.1 and Figure 2.2. show two microscopic views of MPCMs.

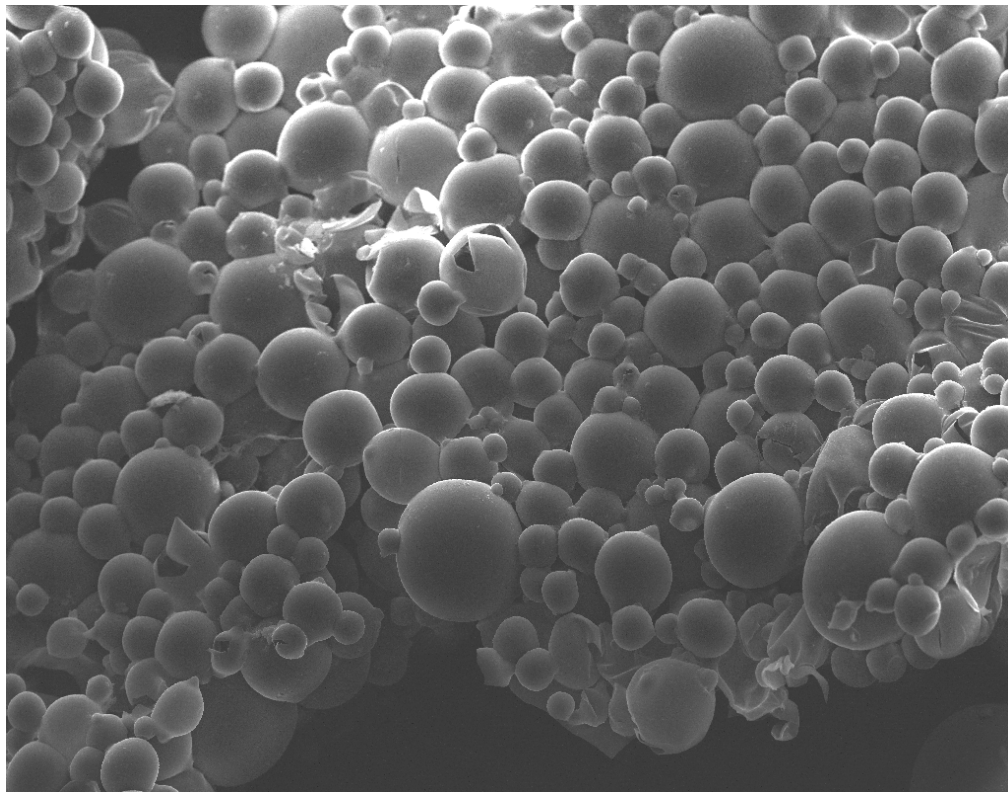


Figure 2.1. Scanning electron micrograph of typical MPCM in water carrier fluid.

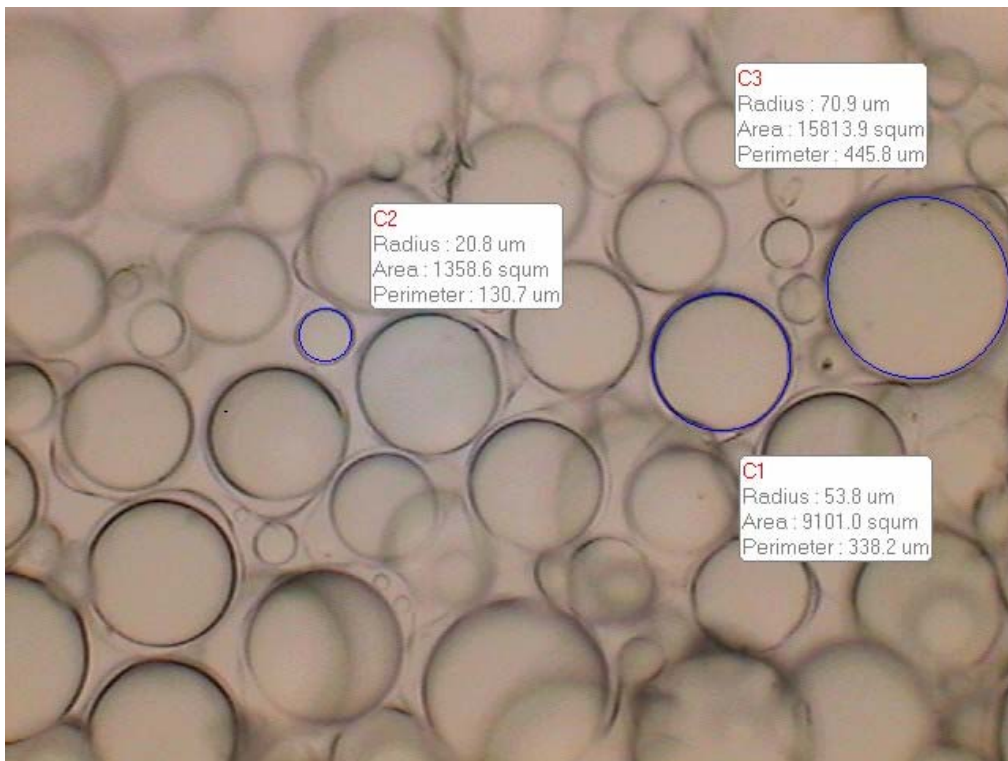


Figure 2.2. Detailed view of MPCMs at 100x magnification.

Few journal articles on MPCM physical properties (as opposed to *free-flowing* phase change materials) have been published. Roy and Sengupta (1991) conducted experiments to evaluate the properties of MPCMs with two characteristic diameters. Differential scanning calorimetry (DSC) was used to determine their thermal properties. Yamagishi et al. (1996) presented experimental results indicating that MPCM particle size does not affect melting temperature and latent heat of fusion. However, the degree of supercooling (i.e., the difference between crystallization and melting temperature) points increased when particle size, d_p , was less than 100 μm . Subsequently, Yamagishi et al. (1996) also tested nucleating agents with molecular structure similar to the PCM molecules and were able to suppress the supercooling effect considerably. Alvarado (2004) conducted a series of experiments and evaluated the thermal properties of tetradecane-containing microcapsules with an average size of 4.4 μm . Yamagishi et al. (1999) obtained empirical data for microencapsulated octadecane obtained using DSC equipment, a Couette viscometer (Yamagishi et al. 1996), and pressure-drop data (Yamagishi et al. 1999). Their results indicate that anionic surfactants can decrease the apparent viscosity of the slurry and transform it into Newtonian-like fluid at high mass fractions (20 – 30%). The results also indicate that the relative viscosity of the MPCM slurry was independent of temperature. As a result, Yamagishi et al. (1999) were able to use the Vand model (Vand 1948) to predict the relative viscosity of the MPCM slurry at different volume fractions.

Ohtsubo et al. (1991) presented experimental data that explained why microcapsules structurally fail. Several experiments show that as D_p/th_p increases, the percentage of broken capsules increases, where D_p and th_p are microcapsule diameter and thickness, respectively.

A limited number of journal articles present and discuss heat transfer and pressure drop characteristics for MPCMs. Goel et al. (1994) describe experiments with MPCMs filled with n-eicosane in which the experimental conditions were limited to laminar flow and constant heat flux. Their results indicate that the Stefan number (St) was the most dominant parameter, especially when St was less than 1.0. Roy and Avanic (1997) showed that laminar forced convection heat transfer characteristics for PCM are similar to MPCM; the capsule walls appear not to have a significant impact on heat transfer. For microcapsules (smaller than 20 μm) filled with n-tetradecane, the calculated Biot number is less than 0.1. Results also indicate that the Reynolds number plays a significant role in the heat transfer process. Yamagishi et al. (1996) experimental data show that MPCM slurry

approximately follows the Blasius equation. They also conducted several heat transfer experiments with uniform heat flux and turbulent conditions. In their research, MPCM particles were filled with octadecane ($C_{18}H_{38}$), and capsule size varied in size between 2 – 10 μm . Results show that as mass fraction increases, turbulent flow changes to laminar, which consequently changes the heat transfer characteristics of the MPCM slurry. Unlike the work documented by Choi et al. (1994), no evidence of pressure drop fluctuations can be found when PCM melts within the MPCM particles, and a constant relative viscosity is observed when the slurry temperature increases (Yamagishi et al. 1996, Alvarado 2004). At high mass fraction, pressure drop decreased, indicating a transformation to laminar flow. One important observation was the effect of particle size on the convective heat transfer coefficient. It is known that particle size (Hestroni 1989) can either enhance or suppress turbulence, which affects momentum and heat transfer. In the case of small MPCMs, turbulence is significantly suppressed (Yamagishi et al. 1999, Alvarado 2004). One significant assumption is that because the microcapsules are small, they melt and solidify instantaneously. Experimental data (Yamagishi et al. 1999, Alvarado 2004) suggest that at an identical heat flux, water has a higher h value than MPCM slurry. It was concluded that changes in h and lower values in viscosity promoted turbulence better in water than in MPCM slurry. Yamagishi et al. (1999) used Choi's model (Choi and Cho 1995) to predict the local Nusselt number, which is defined as:

$$Nu_x = 0.00425 * \left(Re_{bx}^{0.979} Pr_{bx}^{0.4} \left(\frac{\eta_{wx}}{\eta_{bx}} \right)^{-0.11} \right) \quad (2.12)$$

where:

- Nu_x = local Nusselt number
- Re_{bx} = local Reynolds number
- Pr_{bx} = local Prandtl number
- η_{wx} = local wall viscosity
- η_{bx} = local bulk viscosity

They observed that Choi's model could be used to predict after-melting behavior if the single-phase approximation is based on Re_{bx} and Pr_{bx} . However, the model poorly predicted the before- and during-melting Nu_x because MPCM phase change affects C_p and h . Experimental data show that higher heating rate yields lower h , which can be attributed to a thicker boundary layer of melted PCM within the particles. Data also show that at

the same Reynolds number, h increases with mass fraction. It was also evident that higher Reynolds number favors a higher h more than positive changes in mass fraction because higher mass fraction yields higher viscosity and, therefore, suppressed turbulence. In laminar flow, MPCM benefits are limited because solid and melted MPCM segregate around the core fluid, in proximity to the pipe walls (Yamagishi et al. 1999).

Enhanced pipe surfaces

Durmus et al. (2002) present experimental results where snail-type swirl generators were used to augment heat transfer rates by creating swirls in the flow. Results indicate that the Nusselt number (Nu) can be increased by 80% – 200% for 15 – 75 degree swirling angles for air in a counter-flow configuration, but pressure drop increased by 110%. Performance was better when high swirling angles and low Reynolds numbers were used. Fossa and Tagliafico (1995) tested and measured heat transfer rates, with and without smoothed, finned, and grooved pipes, with results indicating that polymeric additives reduce the friction factor but also decrease the Nusselt number. Finned and grooved pipes show a sharper reduction in Nusselt number than smooth pipes for concentrations of 40 ppm and Reynolds numbers between 7,000 and 10,000. Fanning friction factor, f , decreases as compared with pure water only in turbulent flows, by about 25% for finned or grooved pipes and about 20% for smooth pipes. Results also indicate that conductance is greater for finned pipes than for smooth pipes with or without additives. Also, friction factor reduction reaches a minimum at a specific Reynolds number and additive concentration. Liao and Xin (2000) present experimental results on heat transfer and friction characteristics for various liquids with turbulent, transitional, and laminar flow inside a pipe with twisted-tape insert. Results indicate that in turbulent and transitional flows, heat transfer is increased slightly while pressure drop increases significantly. When VG46 turbine oil flow is laminar, the Stanton number is 5.8 times higher when a twisted-tape insert is used instead of a smooth pipe. The friction factor, f , increases 6.5 times also under the same conditions. Stanton number and f with twisted-tape inserts increase with lower tape-twist ratios. Segmented twisted-tape inserts can decrease f by 41 – 44% and Stanton number by 15 – 18% in relation to a continuous twisted-tape insert.

3 MPCM Thermophysical Properties Characterization

Thermal properties determined by differential scanning calorimetry

In order to determine the thermal properties of MPCM, a differential scanning calorimeter (DSC) was used. DSC experiments were carried out to measure the latent heat of fusion and melting point of bulk phase change materials, including tetradecane, pentadecane, and hexadecane. The results from the experiments were used to select which phase change material should be encapsulated. One of the goals was to select a phase change material with the highest heat of fusion value available and a melting point desirable for district cooling applications.

The DSC runs in two modes: conventional and modulated.

In the conventional mode, DSC is used to measure the amount of heat absorbed or released by a sample in comparison with a standard reference. The energy absorbed or released is recorded as a function of time and temperature. The resulting energy/temperature profile curve is used to determine latent heat of fusion, specific heat, and melting point (Charsley and Warrington 1992, Hatakeyama and Quinn 1994, Speyer 1994).

Modulated differential scanning calorimetry (MDSC) is a variation of conventional DSC in which a sinusoidal time-dependent temperature profile is used to control the heating rate as a function of time. The resulting heat flow/temperature profile is interpreted to determine specific heat. The net effect of modulated heat flux is the same as if two experiments were run simultaneously on the specimen.

Figure 3.1 shows a typical endotherm curve extracted from a conventional DSC test of MPCM slurry at 17.4% mass fraction. The melting point is determined by finding the point at which the tangent of the maximum rising slope intercepts the baseline. In this case, the melting temperature (also known as the onset temperature, or transition temperature) occurs at 5.33 °C. The area enclosed by the endotherm curve and the baseline is equivalent to the latent heat of fusion. The crystallization point is found in a similar way as the melting point. If Figure 3.1 were inverted about the

baseline, the crystallization point would be the point at which the tangent of the maximum falling slope intersects the baseline.

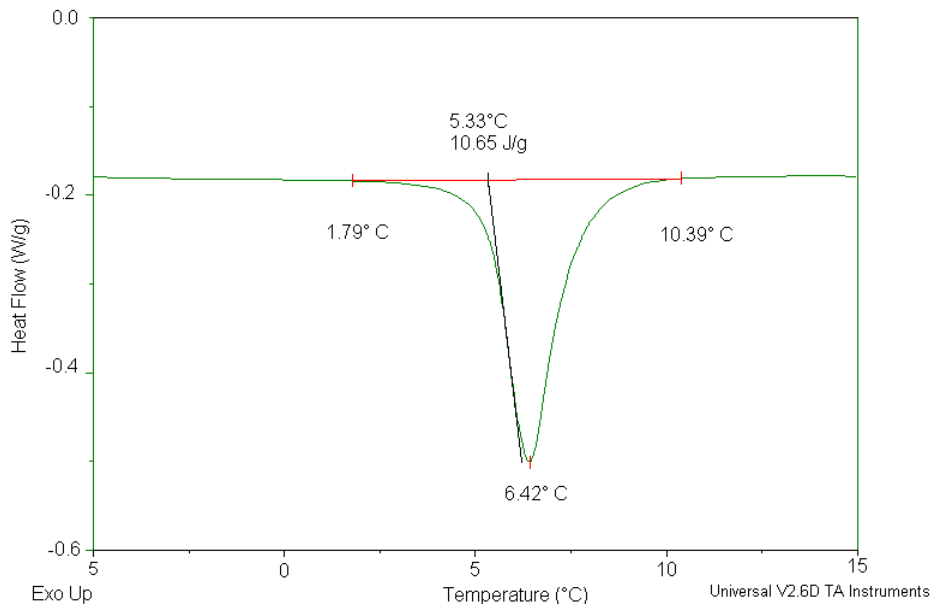


Figure 3.1. Representative DSC endotherm curve.

DSC apparatus and conditions

The thermal behavior of the MPCM slurries under study was recorded using a TA Instruments 2920 Modulated Differential Scanning Calorimeter. Hermetically sealed aluminum pans were used. Helium was used as a purge gas at a flow rate of 26 cm³/min. As part of the calibration process, a baseline calibration run was performed to determine the heat signal when no samples were present. In addition to baseline calibration, cell constant and temperature calibration runs were also conducted. The cell constant value is used as a correction factor to determine how much energy is actually delivered and received by each specimen. Three cell constant calibration runs were performed to accurately measure the amount of heat supplied to the samples and to determine the adjustments necessary for temperature readings and heat flow signal. The values found from each material were within acceptable limits with a combined average value of 1.09. Samples of less than 10 mg of octadecane, water, and indium were used as calibration material. The information collected from the baseline, temperature, and cell constant runs was taken into consideration by the software built into the DSC for computing thermal properties. The built-in software compared the data from the all the calibration runs to determine

the baseline slope, baseline offset, cell constant values, and temperature corrections.

The calibration and experimental runs were performed using a heating rate of 3 °C/min. for all the experiments. The temperature range was kept as narrow as possible to obtain the highest possible resolution. For calibration and MDSC experimental runs, the period of modulation was always set to 100 seconds and the amplitude of modulation was set to 1 °C. Results from all the calibration runs were used for both DSC and MDSC experimental runs.

Water samples of known mass were used to validate the calibration process. All water samples had a mass of 10 mg or less. Eleven samples were tested throughout all the DSC experiments in order to confirm the consistency of the experimental results. The average melting point for the water samples was 0.11 °C. The average value of latent heat of fusion for the same 11 samples was 337.2 J/g, with a standard deviation of 3.8 J/g. The relative error for each sample fluctuated between -2.0% and 1.6%, which eventually averaged to 0.8% relative error. The specific heat of the same 11 water samples also was measured using the DSC equipment in modulated mode, and the average value was within 3.5% relative error. When the average latent heat of fusion is compared with the well established value of 335 J/g, the results of these water sample tests provide confidence that the DSC equipment used in the research can supply reliable, accurate, and consistent data.

All MPCM samples were prepared by using the same experimental procedure. In order to make sure all samples were accurate representations of the bulk slurry, approximately 15 ml of MPCM slurry was placed in a vial and magnetically stirred to assure that all the particles remained in suspension. The same pipette tip was used for all samples, which had an opening large enough to ensure that representative samples were taken every time. All MPCM sample masses were between 9 and 11 mg, consisting of water as the carrier fluid and microcapsules containing PCM. The mass fraction of the MPCM slurry was determined as follows. The initial weight was measured and recorded before the DSC experiment. Following DSC testing, the hermetically sealed container was opened to allow the carrier fluid (water) to evaporate. The sample was then reweighed in order to determine the mass of the MPCMs alone. The MPCM/slurry ratio provides the mass fraction of each sample.

Experimental results

Table 3.1 shows the experimental results from the DSC/MDSC of the three tested PCMs.

Table 3.1. Thermal properties of MPCM based on DSC results.

Phase Change Material	Latent Heat of Fusion, J/g	Melting Point, °C	Crystallization Point, °C
Tetradecane	215.8	5.3	4.6
Pentadecane	160.1	9.3	9.2
Hexadecane	227.1	18.0	16.0

As shown in Table 3.1, tetradecane has a relatively high latent heat of fusion value and a desirable melting point for district cooling applications. As a result, tetradecane was chosen for microencapsulation. In order to avoid any degree of supercooling, a first batch of MPCM containing 0.2% of fumed silica as a nucleating agent was made. The DSC results of the first batch are discussed and illustrated below.

Latent heat of fusion

The results in Figure 3.2 indicate that the MPCM particle latent heat of fusion is directly proportional to mass fraction, which should be expected because tetradecane is the only slurry component undergoing phase change. DSC results in Figure 3.2 also indicate that both MDSC and conventional DSC modes of operation give almost identical results for MPCM capsules ranging 90 – 150 μm in size. The ratio between the latent heats of fusion of microencapsulated n-tetradecane to nonencapsulated n-tetradecane was utilized to determine the average composition of an average MPCM particle. The following relation explains how latent heat of fusion data can be used to determine the bulk composition of MPCM slurry:

$$\frac{\text{Mass}_{\text{MPCM}}}{\text{Mass of Average Microcapsule}} = \frac{\text{LHF of Microencapsulated PCM Slurry Sample}}{\text{MF}_{\text{MPCM}} * \text{LHF of Non - encapsulated PCM}} \quad (3.1)$$

where:

$\text{Mass}_{\text{MPCM}}$ = mass of MPCM within an average microcapsule

MF_{MPCM} = mass fraction of MPCM sample

LHF = latent heat of fusion of PCM

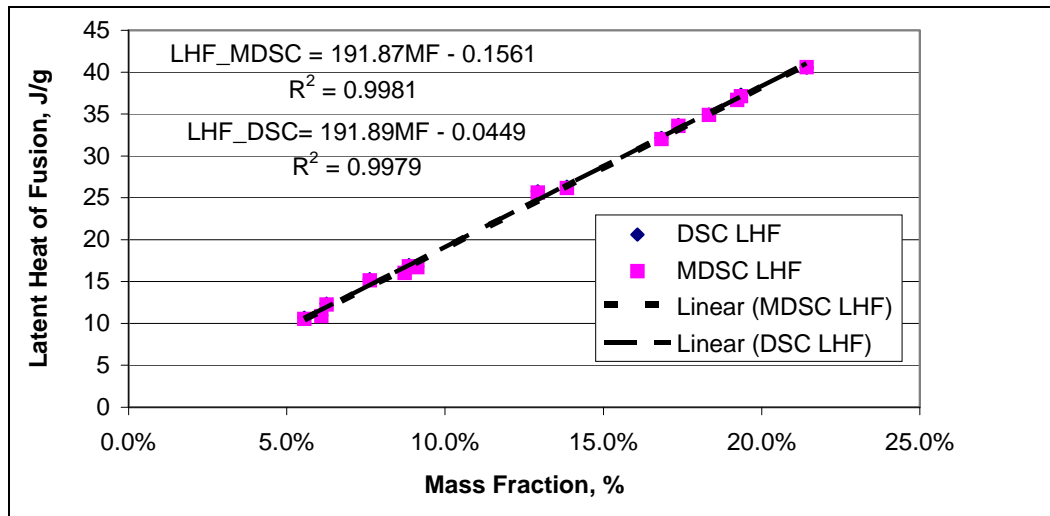


Figure 3.2. Latent heat of fusion of MPCM slurry (90 – 150 μm).

It should be noted that the mass of an average microcapsule is equal to the mass of microencapsulated PCM and the mass of the microcapsule wall material and nucleating agent.

The experimental data show that an average MPCM particle consists of 88.3% of n-tetradecane and 11.7% of microcapsule wall material.

Specific heat

The MDSC data suggest, as shown in Figure 3.3, that specific heat is not a strong function of mass fraction, which seems to contradict previous findings (Yamagishi et al. 1999). However, if it is taken into account that (1) the highest MPCM mass fraction tested was less than 20%, (2) the difference in specific heat values between n-tetradecane and water was less than 47%, and (3) the DSC equipment provides specific heat values within a 3.5% margin of error, it then becomes clear that the results shown in Figure 3.3 are confounded with the observed experimental error as depicted by the vertical error bars. In other words, when experimental error is accounted for, a slight decrease in MPCM slurry heat, as a function of mass or loading fraction, is suggested but not definitely demonstrated. Nonetheless, it is at best a weak dependence, in contrast to the more marked function as reported by other researchers.

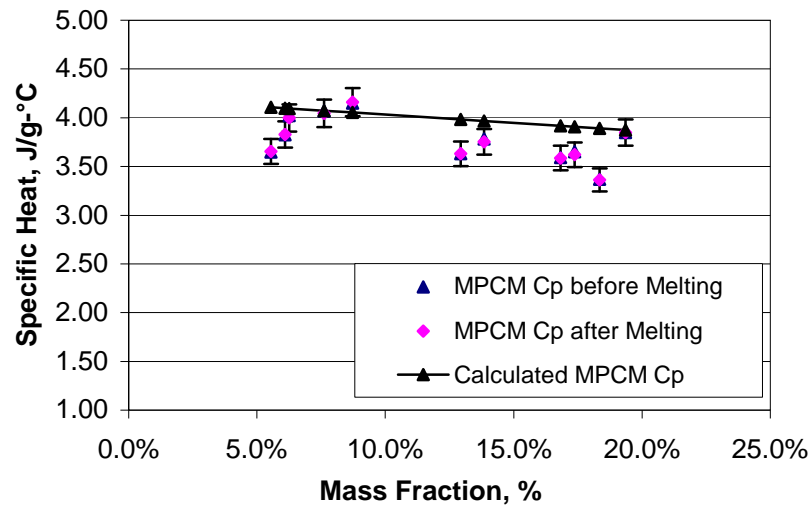


Figure 3.3. Specific heat of MPCM slurry (90 – 150 μm).

Melting and crystallization points

Another group of thermal properties that is important in experimentation and application are the melting and crystallization (i.e., freezing) points of the microencapsulated tetradecane. Under ideal equilibrium conditions, the melting and freezing points of MPCM should be identical. However, due to the size of the MPCM particles and finite cooling rates (1 – 9 $^{\circ}\text{C}/\text{min}$), MPCM particles exhibit a measure of supercooling regardless of mass fraction, as indicated in Figure 3.4. Supercooling occurs in the region between the material's freezing and melting temperatures. Figure 3.4 clearly shows that the amount of supercooling for microencapsulated tetradecane containing 0.2% fumed silica is still significant, and this is highly undesirable because the melting and crystallization temperatures of the carrier fluid are 0 $^{\circ}\text{C}$. Consequently, considerable effort was applied to understand the nature of supercooling in microcapsules. Most knowledge about supercooling has been provided by classical nucleation theory (CNT) and several experimental results published in the last 20 years.

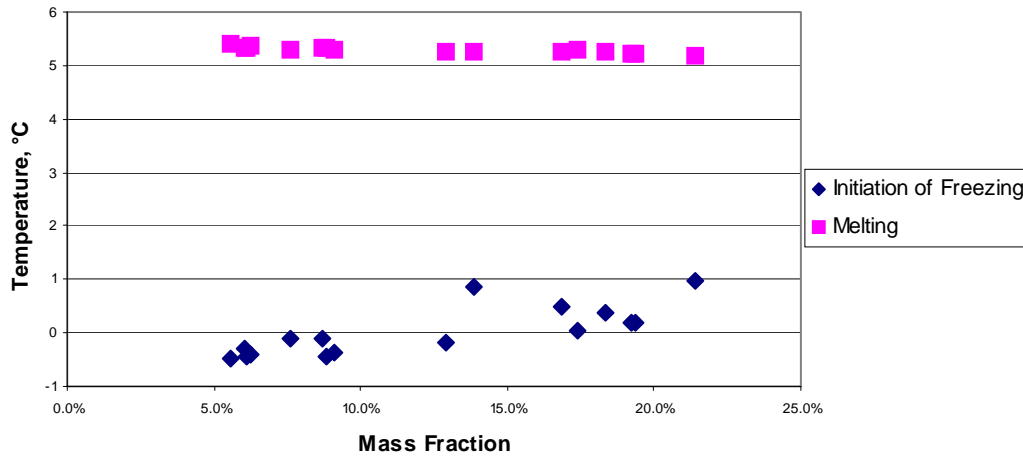


Figure 3.4. Melting and initiation of freezing points of MPCM slurry (90 – 150 μm).

Nucleation issues

Classical nucleation theory (CNT) asserts that liquid-to-solid transformations take place because of a homogeneous or heterogeneous nucleation mechanism. Homogeneous nucleation relies on the formation and growth of stable nuclei within the microcapsule, while heterogeneous nucleation is basically a surface-mediated mechanism. It is known that homogeneous nucleation has a greater nucleation barrier than heterogeneous nucleation and causes greater supercooling or requires a lower temperature for stable nuclei to form and grow (Montenegro et al. 2003). Montenegro and Landfester (2003) found that nanodroplets (125 – 500 nm) showed a considerable degree of supercooling, indicating homogeneous nucleation as the predominant type of nucleation mechanism. Most recent experimental data also show that the temperature at which freezing occurs does depend on particle size (Yamagishi et al. 1996, Montenegro et al. 2003).

Yamagishi et al. (1996) encountered similar difficulties in suppressing supercooling and used paraffin-like molecules with higher melting points than their homologous molecules as nucleating agents. The results shown in Figure 3.5 suggest that the right kind and amount of nucleating agent must be carefully chosen to control the supercooling phenomenon effectively. In order to determine the right kind and amount of nucleating agent for microencapsulated tetradecane, bulk mixtures of tetradecane and tetradecanol at different ratios were tested using DSC. Figure 3.6 shows the DSC results for different concentrations of tetradecanol in tetradecane. In bulk samples, 2% tetradecanol was sufficient to suppress supercooling almost entirely. Based on that result, a second batch of MPCM was made containing 98% tetradecane and 2% tetradecanol.

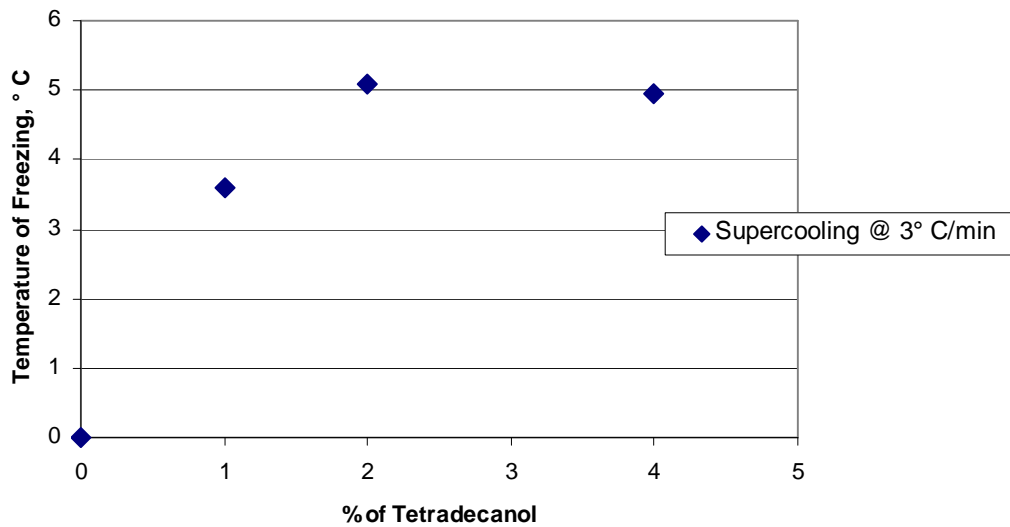


Figure 3.5. Degree of supercooling as a function of tetradecanol in tetradecane

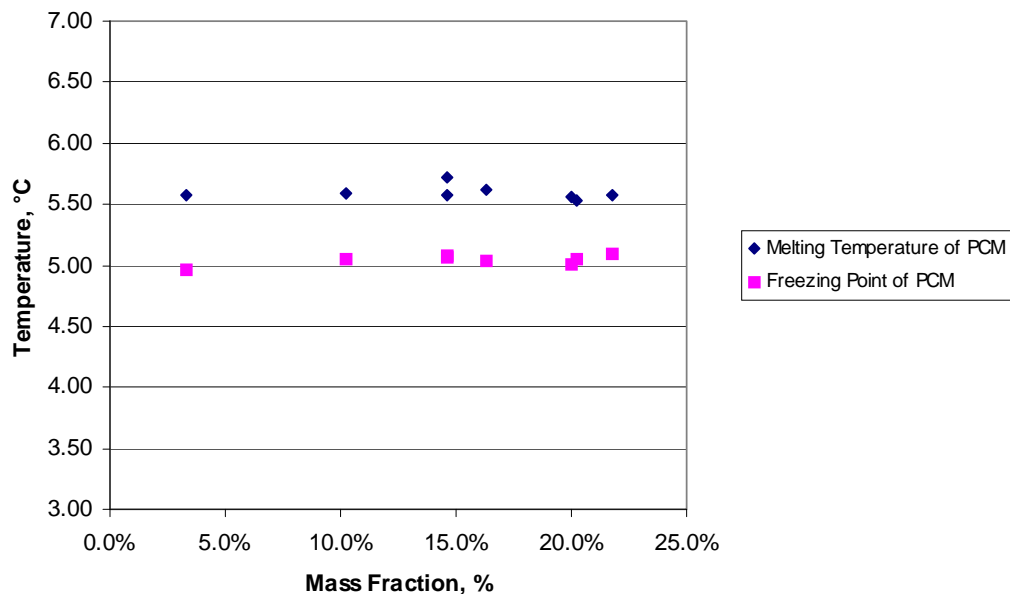


Figure 3.6. Melting and freezing points of microencapsulated n-tetradecane with 2% tetradecanol (70 – 260 μ m).

Figure 3.7 shows the DSC results for MPCM 70 – 260 μ m in diameter containing 98% tetradecane and 2% tetradecanol. The results indicated that the degree of supercooling was considerably lower than for the first batch, and ideal for further testing. However, durability test results (see page 36) indicated that the second batch was unsuitable for further testing.

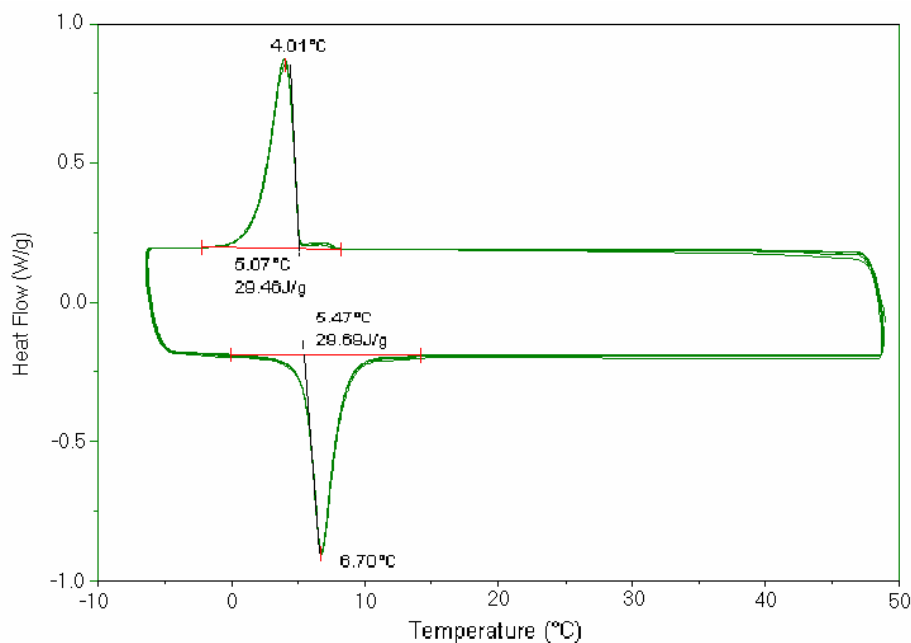


Figure 3.7. Thermal cycling of MPCM with 2% tetradecanol.

In order to ensure the long-term reliability of tetradecanol to perform as a nucleating agent, thermal cycling tests were conducted in which the temperature of an MPCM sample was raised above 45 °C, as shown in Figure 3.7. The melting point of tetradecanol is approximately 37.9 °C. Figure 3.7 clearly demonstrates that the nucleating agent is able to consistently perform this function for multiple cycles. (Five cycles are shown in the figure.)

A third and fourth batch of MPCM were made containing 96% tetradecane and 4% tetradecanol, and 96% pentadecane and 4% pentadecanol, respectively. The microcapsules in both batches varied between 5 – 20 µm in diameter. DSC results for both batches are shown in Table 3.2.

Table 3.2. DSC results for third and four MPCM batches (5 – 20 µm).

Microencapsulated Phase Change Material	Melting Temperature, °C	Crystallization Temperature, °C	Supercooling, °C
96% tetradecane + 4% tetradecanol	5.0	2.0	3.0
96% pentadecane + 4% pentadecanol	9.8	9.3	0.5

The results shown in Table 3.2 support previous findings that microcapsule size does have an impact on PCM crystallization temperature. However, due to durability problems in larger capsules (over 100 µm), capsule size should be smaller than 20 mm. More discussion of capsule durability is presented later in this chapter.

Chemical compatibility of capsule and anti-freezing additives

Several anti-freezing compounds were selected for use in the MPCM in an attempt to lower the starting freezing point of the MPCM. The temperature at which freezing initiates is shown to increase with an increasing mass fraction of MPCMs, which results in a lower freezing point for the carrier fluid. Unfortunately, there are a disadvantages of this approach that outweigh the benefits. Disadvantages include an increase in viscosity for both turbulent and laminar flows, lower heat transfer due to reduced conductivity and convection resulting from the higher viscosity, increased osmotic pressure, and lower efficiency. The tested anti-freezing additives are shown in Figure 3.3 along with their recorded parameters.

Table 3.3. Various compounds used as anti-freeze agents.

Name	% Concentration for freezing point at -6.7 °C	Viscosity, cP*	pH	Color Change	MPCM Integrity
Potassium Hydroxide	9.6	1.22	14.0		Dissolved
Sodium Nitrate	17	1.2	7.1		OK
Sodium Hydroxide	7	1.5	13.5		Dissolved
Sodium Chloride	10.5	2.8	7.8		OK
Calcium Chloride	11	3.0	4.6	Darker	OK
Sodium Acetate	13.3	1.8	9.8		OK
Methanol	10.2	4.5	4.7		OK
Ethylene Glycol	18	4.5	4.0	No Change	OK
Potassium Formate	11	2.72	6.0		OK
MPCM @ 20%	-	-	4.8		OK
Water @ 0.01 °C		1.79			

cP: centipoises; 1 cP = 0.001 pascal.

Of the nine agents investigated as an antifreeze, two (potassium hydroxide and sodium hydroxide) were not suitable because they are highly alkaline and dissolved the microcapsule surrounding the PCM. The anti-freezing agents were mixed with the MPCMs and rotated for 10 days before the visual inspection. Methanol was studied further, and Figure 3.8 shows the viscosity as a function of concentration for temperatures 0 – 20 °C. A magnified image of the methanol/MPCM slurry is shown in Figure 3.9.

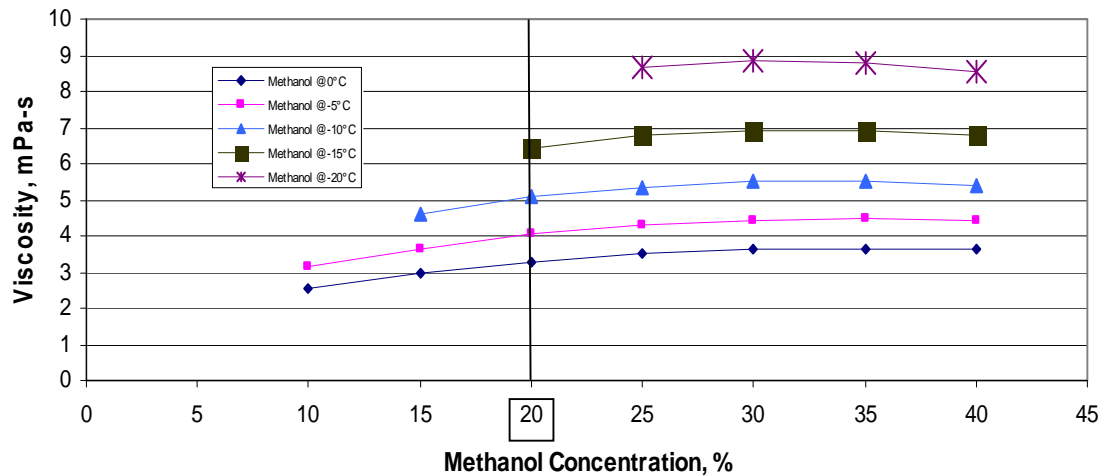


Figure 3.8. Methanol/water mixture viscosity as a function of concentration (lower concentration regions disallowed for freezing).

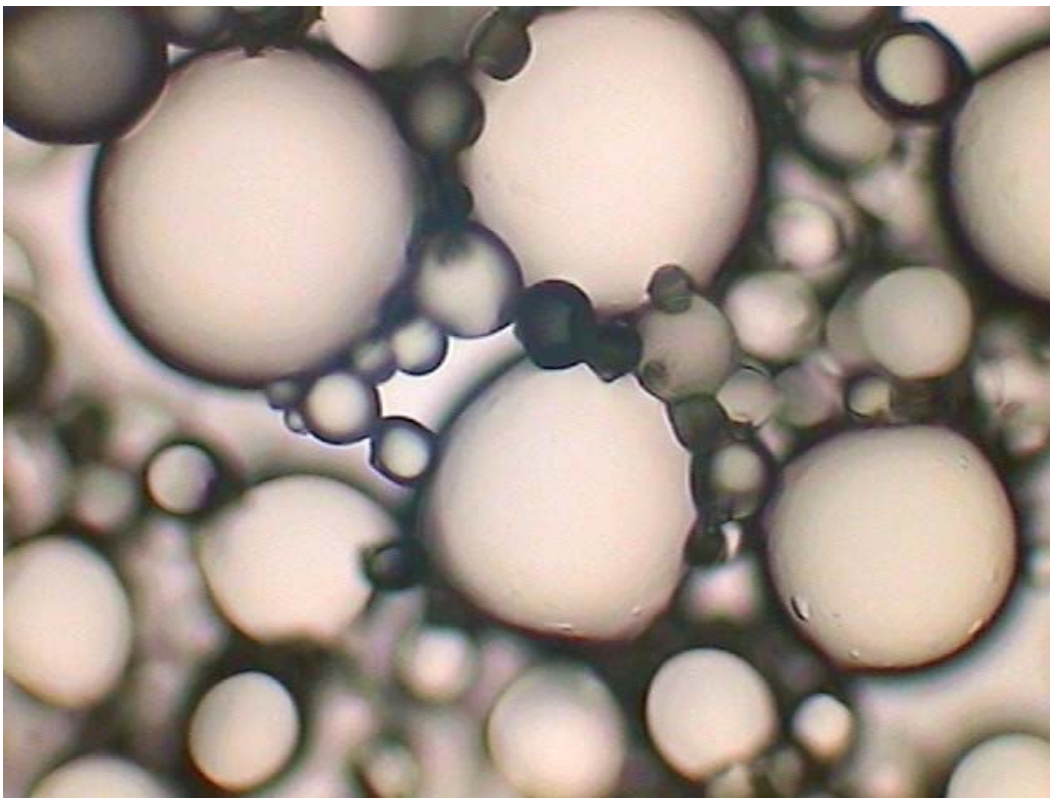


Figure 3.9. MPCMs after 10 days in methanol mixture (20%), 100x magnification.

Viscosity measurements

Previous studies have investigated, described, and reported on how spherical particles affect the apparent viscosity of slurries. Vand (1948) studied the interactions among particles in liquids and proposed a model that has since been used as the basis for the study of slurry viscosity. The

Vand model couples the hydrodynamic equations governing incompressible flow around a rigid sphere with the effect of sphere-sphere interactions. The Vand model describes the increase in suspension viscosity due to the presence of the hard spheres as follows:

$$\eta = \eta_w e^{\frac{k_e \phi_{sphere}}{1 - \lambda \phi_{sphere}}} \quad (3.2)$$

where:

$k_e = 2.5$, Einstein's shape factor for single spheres

$\lambda = 0.609375$, the hydrodynamic interaction constant

ϕ_{sphere} = volume fraction of the rigid spheres.

Thomas (1965) also studied particle liquids in detail and proposed viscosity models that depend on volume fraction for dilute and concentrated suspensions. Yamagishi et al. (1996) presented viscosity data acquired from several experiments by using a cylindrical Couette viscometer and pressure drop measurements. In that study, the apparent viscosity of MPCM slurry clearly showed a Newtonian fluid behavior when a 1% anionic surfactant was used. A later study (Yamagishi et al. 1999) showed that the relative viscosity of MPCM slurry was fairly independent of temperature, suggesting a strong correlation with changes in the viscosity of pure water.

Absolute viscosity was another important physical property that was measured in order to design the experimental heat transfer test loop and predict subsequent experimental conditions. A temperature-controlled concentric viscometer was used to determine the apparent viscosity of MPCM slurry. A typical concentric viscometer consists of a rotating cylinder or spindle contained inside a temperature-controlled vessel. The cylinder spins at constant and discrete rotational speeds, and the viscosity of a sample is determined by measuring the torque exerted by the fluid against the rotating cylinder. A Brookfield viscometer, model LVT with an ultra-low (UL) adapter, was used to measure the viscosity of the MPCM slurry. For temperature control, the container or UL adapter was connected to a water bath that circulated water at a fixed temperature. A solution of laboratory-grade propylene glycol-water mixture at 34.6% and known viscosity values was prepared to calibrate the viscometer. The viscometer was cali-

brated at different temperatures and spindle rotational velocities after the system had reached a constant temperature for at least 30 minutes. It was determined that the viscometer was within a 1% margin of error as suggested by the viscometer manufacturer.

The viscosity of MPCM samples of different mass fractions was measured at 12, 30, and 60 revolutions per minute to determine if the slurry behaved as a Newtonian fluid. Each sample was in the UL adapter for 30 minutes and stirred magnetically to make sure all the microcapsules were uniformly suspended before measuring the viscosity. Three measurements were taken for every sample. The mass fraction of each sample was determined by taking three aliquots of MPCM slurry (approximately 20 μl each) from the UL adapter. Each aliquot was dried to determine the water content and mass fraction of the sample. Statistical analysis was used to determine which set of data points was suitable for further analysis. Figure 3.10 and Figure 3.11 show the statistically significant viscosity results.

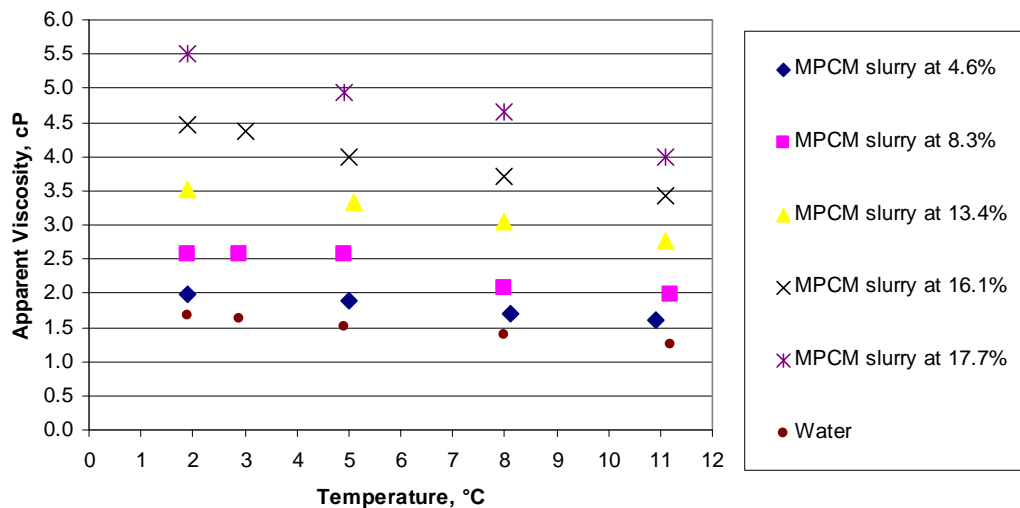


Figure 3.10. Apparent viscosity of MPCM slurry as function of mass fraction and temperature (5 – 20 μm).

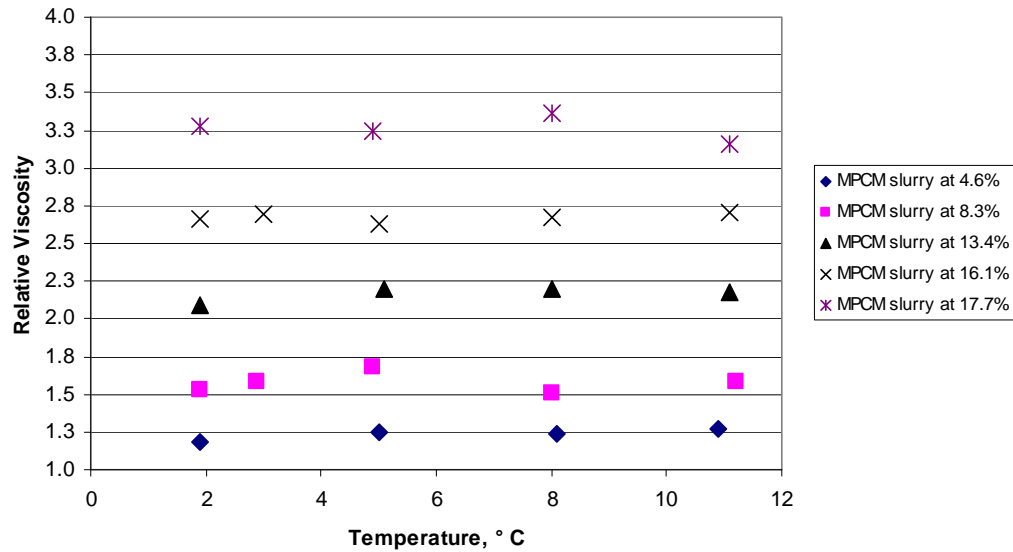


Figure 3.11. Relative viscosity of MPCM slurry as function of mass fraction and temperature (5 – 20 μm).

Figure 3.10 illustrates the dependence of apparent viscosity on temperature and mass fraction. It is also to be noted that viscosity dependence on temperature is stronger at higher mass fractions. However, the relative viscosity of MPCM slurry shown in Figure 3.11 seems to be independent of temperature regardless of mass fractions, reaffirming the findings and results presented by Yamagishi et al. (1999). Relative viscosity is defined as the ratio between the apparent viscosity of MPCM slurry to that of water at a given temperature. Thomas (1965) analyzed several experimental results reported earlier and noted lower relative viscosity for the same mass fraction shown in Figure 3.11. However, Yamagishi et al. (1999) also found that MPCM slurry has a higher relative viscosity than the data collected and analyzed by Thomas (1965) indicate but comparable to the data depicted in Figure 3.11, suggesting that microcapsule shape and rigidity may be playing a role in increasing relative viscosity (Yamagishi et al. 1999). The MPCM viscosity results also indicate that MPCM slurry behaves as a Newtonian fluid at least up to 17.7% of mass fraction.

The impact of higher viscosity at lower temperature and higher mass fraction should also be taken into consideration when selecting operating conditions or sizing equipment because higher viscosity implies higher pumping power, lower turbulence, and lower thermal conductivity, each of which could reduce local heat transfer rates in the absence of phase change behavior. The data depicted in Figure 3.10 and Figure 3.11 can also be used for thermal system simulations to estimate level of turbulence in the

slurry. As an investigative study (Appendix A) provides detail on the formulation of a viscosity model that includes both loading fraction and temperature.

Durability testing

In order for MPCMs to effectively be used in general application, they must be able to withstand constant pumping within the system and any degree of turbulence inherent in the particle flow. Several batches of MPCM particles were subjected to a series of durability tests. A durability test loop was constructed to determine what percentage of a fixed amount of MPCM slurry can survive continuous pumping and surface friction losses. The device consisted of a closed loop made of copper tubing that varied in diameter from 3/8 to 1 in. A Moyno progressing cavity pump was previously found to handle viscous slurries while causing the least amount of damage to the MPCM particles (Yamagishi et al. 1996), so it was selected to pump the system in the current work. Figure 3.12 shows a schematic representation of the durability loop.

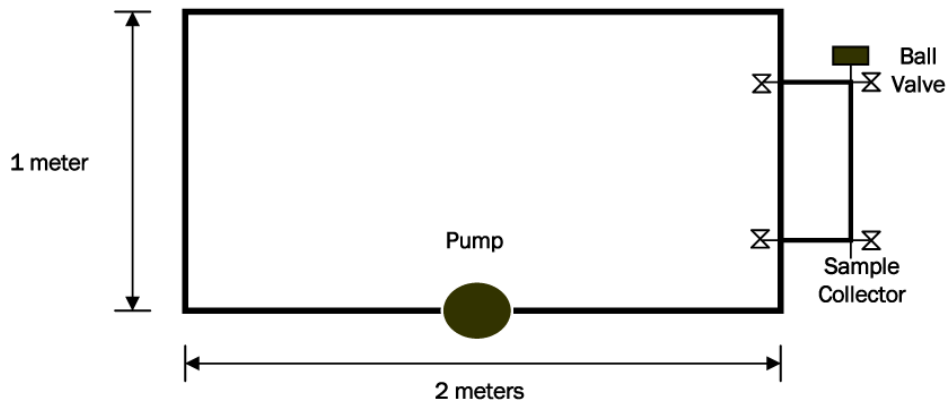


Figure 3.12. Schematic representation of durability loop.

Periodic samples were taken and submitted to examination. First, samples were examined by using a professional-quality optical microscope at magnifications varying between 40 – 1000x to look for any physical damage. Second, the total amount of released or free tetradecane was determined by using a filtration device to separate the liquid phase (including any free tetradecane) from the solid phase (unbroken microcapsules), and measuring the amount of free tetradecane in comparison with the total sample volume. If the durability test yielded 10% or more broken capsules, smaller capsules or capsules with greater thickness-to-diameter ratio were tested, as suggested by Ohtsubo et al. (1991).

As part of the durability test procedure, different experimental conditions were used as summarized in Table 3.4. In order to determine the impact of fluid velocity and level of turbulence on the durability of the microcapsules, each MPCM batch was tested with increasingly turbulent conditions, beginning from 1 – 8 ft/sec. Three batches of different MPCM size range were tested, and the results are summarized in Table 3.5.

The results shown in Table 3.5 are consistent with the results published by Yamagishi et al. (1996), which claim that microcapsule size is the main factor affecting durability. The durability results clearly indicate that the smallest microcapsules (5 – 20 μm) show the least degree of damage, and therefore are the most suitable for further experimentation. The results also show that after 1,200 cycles through the progressing pump (third batch), no significant amount of microcapsule breakage or surface wear was detected.

Table 3.4. Experimental conditions for durability tests.

Mass Fraction = 20%							
Velocity at 3/8" section, ft/sec	Circulation Times	Accumulative Circulation Times	Time, hrs	Accumulative Time, hrs	Viscosity ¹ , mPa-sec	Density ¹ , kg/m ³	Reynolds Number
1	100	100	2.15	2.15	5	937.5	545
2	100	200	1.08	3.23	5	937.5	1089
4	100	300	0.55	3.78	5	937.5	2179
6	100	400	0.37	4.15	5	937.5	3268
8	400	800	1.09	5.24	5	937.5	4357

Mass Fraction = 5%							
Velocity at 3/8" section, ft/sec	Circulation Times	Accumulative Circulation Times	Time, hrs	Accumulative Time, hrs	Viscosity ¹ , mPa-sec	Density ¹ , kg/m ³	Reynolds Number
8	400	1200	1.09	6.34	2	983.6	11428

¹ Values are approximate.

Table 3.5. Results from durability experiments.

Batch Number	MPCM Size Range (μm)	Total Time of Durability Test, hrs ¹	% of Broken Microcapsules	Experimental Conditions	Accumulative Circulation Times
1	90-150	9.7	15.5%	2 - 8 ft/sec	700
2	70-260	5	16%	2 ft/sec	400
3	5-20	7	0% ²	2 - 8 ft/sec	1200

Notes: Total time includes cumulative results for the same batch at low and high mass fraction. No significant amount of free or released tetradecane was detected (within 2% margin of error).

4 Heat Transfer Characterization of MPCM Slurry

Experimental system design

A heat transfer section was designed to measure the convective heat transfer and pressure drop of MPCM slurry before, during, and after the phase change material has undergone a solid-to-liquid transformation. To achieve fully turbulent conditions at different MPCM slurry mass fractions, the Reynolds number was calculated taking into account pipe diameter, fluid velocities between 0.6 – 2.4 m/sec, and the measured slurry viscosity.

Heat transfer section

A 12.2 meter (40 ft) long heat transfer section was constructed and tested to be able to determine the convective heat transfer coefficient and pressure drop of MPCM slurry. The length of the copper tubing was specified to guarantee a full phase change transition as well as hydrodynamic and thermal entry length requirements. The section consisted of eight 1.52 meter (5 ft) long subsections made of 10.9 mm (3/8 in.) copper tubing. Each subsection had a total of five Type T thermocouples soldered to the outer surface at 30.5, 61, 76.2, 91.4, and 121.9 cm (12, 24, 30, 36, and 48 in.) from either end of the subsection. Each tubing subsection was then coated with plastic paint to minimize electrical conduction. A 24 gauge insulated nickel-chromium resistance wire was coiled around the copper tubing to provide constant heat flux. Each tubing subsection had three independent resistance wire sections all connected in parallel. The entire heat transfer section consisted of 24 independent resistance wire sections all connected in parallel to ensure constant heat flux. Additional resistance wire was added as external resistance was needed to match the desired overall heat flux. The additional resistance wire was connected by using ceramic terminal blocks that were not in direct contact with the tubing sections. A thick layer of fiberglass insulation was used to thermally insulate each subsection.

All tubing subsections were aligned horizontally by using a laser level. A Moyno progressing cavity pump was used to pump the slurry through the system. An Omega magnetic flow meter was used to measure fluid velocity

to an accuracy of 0.5%. The performance of the magnetic flow meter was validated by performing a simple bucket-watch experiment with water. Also, an ultrasonic flow meter with an accuracy of 2% was used to corroborate the readings given by the magnetic flow meter. Three Cole-Parmer pressure differential transducers were used to measure pressure drop. Each pressure transducer could detect up to 17.2 kPa (2.5 psig) with 0.25% accuracy of the full range. Two variable-voltage alternating current transformers (variacs) were used as power supplies. Each could provide 0 – 208 v. For data logging, an Agilent data logger (34970A Data Acquisition/Switch Unit) with three multiplexer cards was used to record temperature and pressure drop. An independent power meter was used to measure total power consumption as well as current and voltage delivered by each transformer.

The last subsection of the heat transfer loop was interchangeable, which allowed for changes in pipe diameter or tubing material. In addition to using 10.9 mm (3/8-inch) copper tubing, soft copper and enhanced copper tubing of 8 mm diameter was also used to determine the impact of $D_{\text{pipe}}/d_{\text{particle}}$ ratio and tubing roughness (or enhancement) on the heat transfer process. The enhanced tubing section incorporated helical microfins of 200 μm in height and width, with about 60 microfins around the circumference. The orientation of the microfins with respect to the longitudinal axis was 18 degrees.

A water-ice bath was used as the cooling medium to force the MPCM to undergo a liquid-to-solid transformation. Two compact heat exchangers were used to provide enough heat transfer area to ensure full phase change. A simple schematic of the entire system is shown in Figure 4.1.

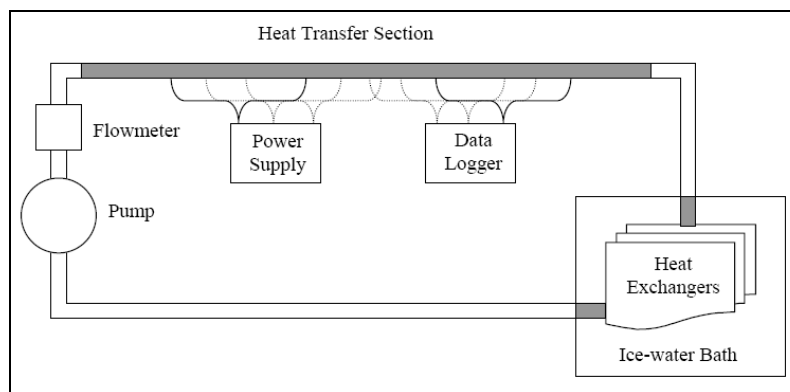


Figure 4.1. Schematic of heat transfer loop.

Calibration of the thermocouples was performed in situ. Based on the recorded and scanned temperature values, appropriate and acceptable offset and gain values were determined for each thermocouple, all within 10% of the noncalibrated settings. Several heat transfer experiments with plain water were conducted to validate the calibration procedures. The following sections explain in detail the validation procedure and results.

Water pressure drop test

Pressure drop data were analyzed and compared with the Darcy-Weisbach equation (Equation 4.1), the Colebrook correlation for friction factor (Equation 4.2), and the steady-flow energy equation (4.3):

The Darcy-Weisbach equation is:

$$h_f = f \frac{L V^2}{d 2g}, \quad (4.1)$$

where f , L , d , V , and g are the friction factor, pipe length, pipe diameter, fluid velocity, and gravitational constant, respectively.

The Colebrook equation (ASHRAE Handbook 2001) is:

$$\frac{1}{\sqrt{f}} = 1.14 + 2 \log\left(\frac{D}{\varepsilon}\right) - 2 \log\left[1 + \frac{9.3}{\text{Re}\left(\frac{\varepsilon}{D}\right)\sqrt{f}}\right] \text{ for } \text{Re} > 3000 \quad (4.2)$$

where f , ε/D , and Re are the friction factor, relative roughness, and Reynolds number, respectively.

The steady-flow energy equation (for horizontal pipes) is:

$$h_f = \frac{\Delta P}{\rho g} \quad (4.3)$$

where h_f , ΔP , ρ , and g are friction head loss, pressure drop, fluid density, gravitational constant, respectively.

Three wet-to-wet differential pressure transducers from Cole-Parmer were used to measure pressure drop at several velocities and slurry concentra-

tions. The pressure transducers were calibrated using the specifications provided by the manufacturer. The calibration results were validated using water. The pressure transducers generated a current signal that was converted to pressure units by the Agilent data acquisition unit.

The validation results indicate good agreement with the calculated results for the same flow conditions assuming smooth tubing surface (within 8% relative error). The results from the pressure drop test using enhanced tubing were compared with simulated and calculated results based on the Colebrook equation. Simulated results were based on the standard roughness factor (ϵ) for copper tubing and 0.2 mm for the enhanced tubing to account for the microfin enhancement size.

Figure 4.2 suggests that a roughness factor value for an 8 mm enhanced tubing section falls between the characteristic value for smooth copper tubing and a roughness value of 0.2 mm. As per the Colebrook equations, a roughness factor of 0.1 mm seems to reasonably match the pressure drop profile of the enhanced tubing.

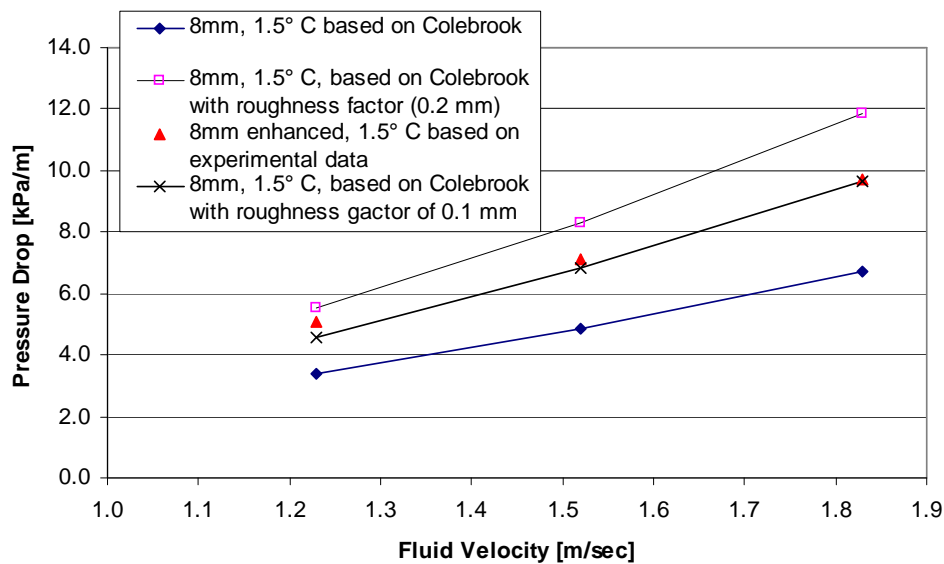


Figure 4.2. Pressure drop of water with 8 mm enhanced tubing.

MPCM slurry pressure drop test

Several pressure tests were conducted to determine pressure drop of MPCM slurry at two mass fractions. Pressure drop data were collected when the slurry reached steady-state temperature and flow conditions. Figure 4.3 shows the results from a pressure drop test at low mass fraction ($5.9\% \pm 0.4\%$). Figure 4.3 also shows a simulated pressure drop profile for

water based on the Colebrook equation at the same flow conditions as for the MPCM slurry. The results indicate that the pressure drop increases slightly when MPCM particles are used, but not significantly enough to affect pumping power.

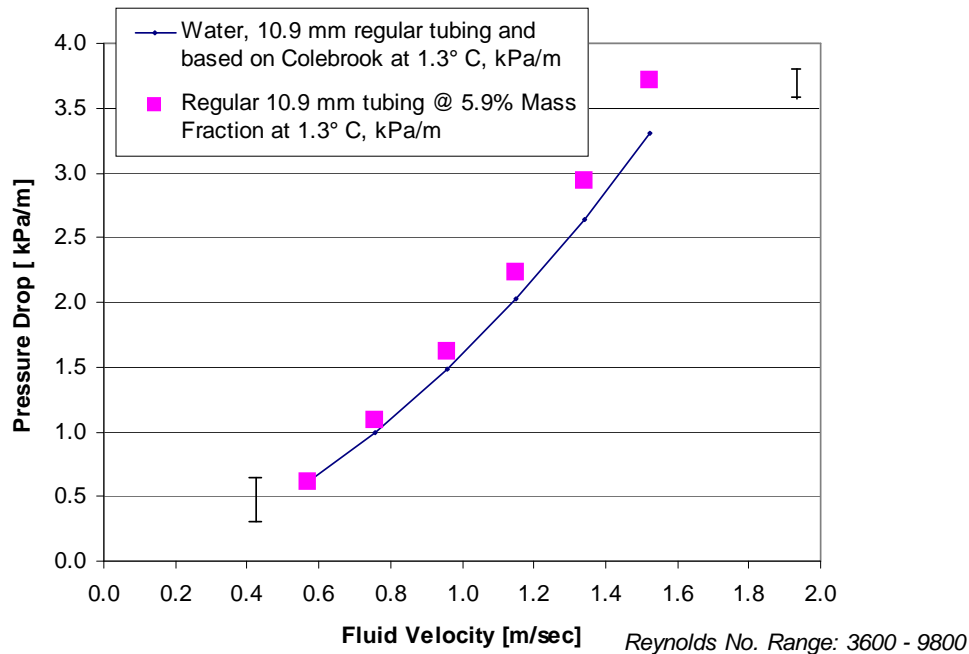


Figure 4.3. Pressure drop of MPCM slurry at 5.9% mass fraction, 10.9 mm regular tubing.

Figure 4.4 shows pressure drop results at 5.9% ($\pm 0.4\%$) mass fraction when 8 mm smooth and 8 mm enhanced tubing sections were tested. Pressure drop for MPCM slurry is lower than a simulated pressure drop profile for water based on the Colebrook equation and an 8 mm smooth tubing section. Figure 4.4 also reveals that enhanced and smooth tubing sections display similar pressure drop behavior and magnitude. The plot also shows that the experimental pressure drop for water is greater than for the MPCM slurry at 5.9% mass fraction when enhanced tubing was tested. The results may suggest that a small amount of microcapsules ruptured and released phase change material into the carrier fluid, creating favorable conditions for a drag-reducing effect (Kostic 1994). Samples were taken and examined for broken capsules or released tetradecane within a 2% margin of error. No significant amount of tetradecane could be detected and micrographs did not reveal the presence of broken capsules. It is plausible that the microencapsulation process produced a small amount of aggregates (not fully formed capsules) that were susceptible to early breakage. Visual inspection of the entire batch did not reveal any significant amount of free tetradecane at the surface of a 10-liter container, so

only a small of free tretadecane might have remained in solution. It is plausible that a small amount of free tetradecane could have cancelled any drag effect associated with the enhanced surface (Fossa and Tagliafico 1995). Fossa and Tagliafico (1995) observed significant drag reduction or friction coefficient reduction (5 – 25%) when long-chain molecules in concentrations from 5 – 40 ppm were tested in combination with tubing that had helical groove enhancements.

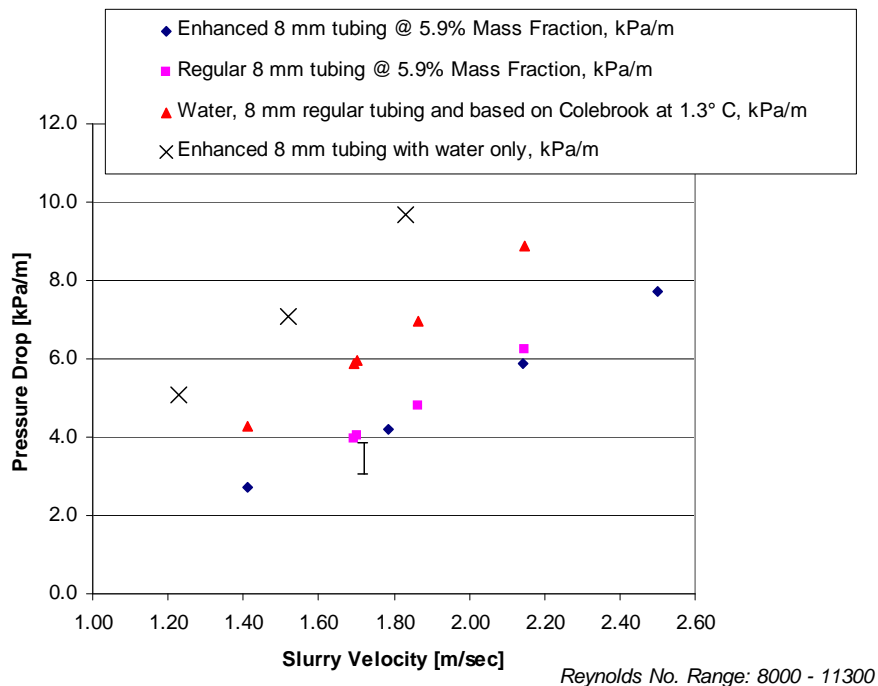


Figure 4.4. Pressure drop of MPCM slurry at 5.9% mass fraction, 8 mm regular and 8 mm enhanced tubing.

Figure 4.5 and Figure 4.6 show pressure drop results at 13.4% and 15.2% ($\pm 0.4\%$) mass fractions when 10.9 mm and 8 mm smooth tubing, and 8 mm enhanced tubing were tested. Pressure drop for MPCM slurry at 15.2% mass fraction is relatively higher than a simulated pressure drop profile for water based on the Colebrook equation when a 10.9 mm tubing section was used. However, lower pressure drop was observed when smooth and enhanced 8 mm tubing sections were used. The results are consistent with the pressure drop results at low mass fractions, suggesting that the same mechanisms are also in play at higher mass fractions.

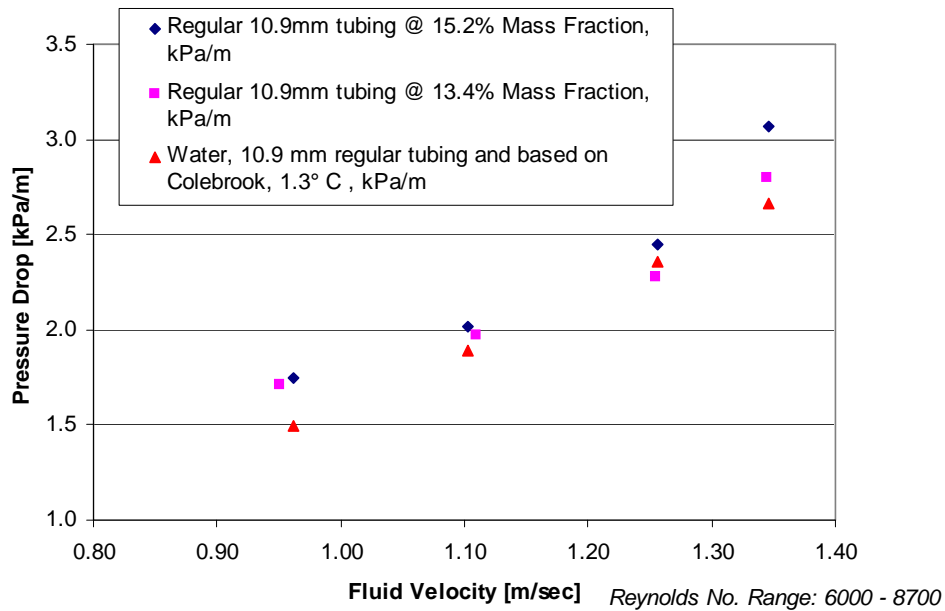


Figure 4.5. Pressure drop of MPCM slurry at 13.4% and 15.2% mass fraction, 10.9 mm smooth tubing.

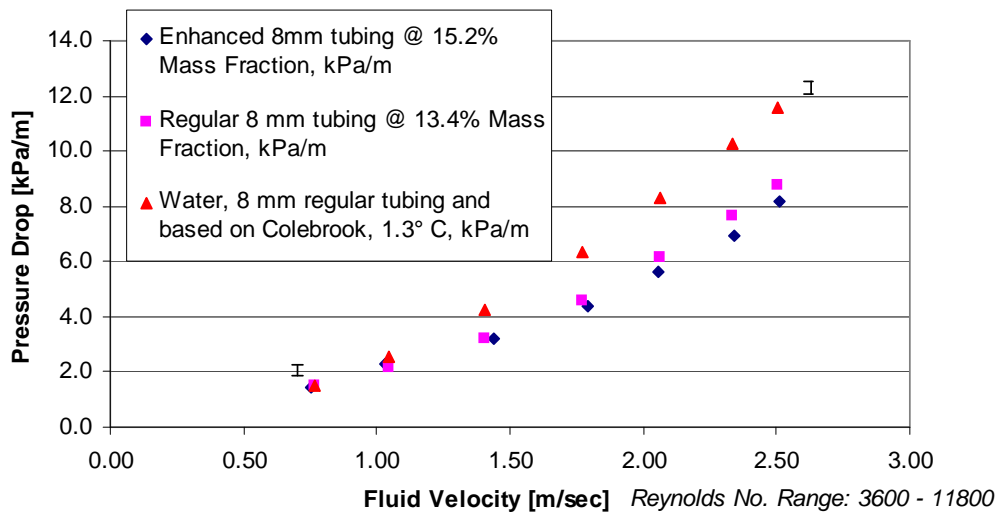


Figure 4.6. Pressure drop of MPCM slurry at 13.4% and 15.2% mass fraction, 8 mm smooth, and 8 mm enhanced tubing.

As seen in all cases, pressure drop does not increase with particle loading, suggesting that a drag-reducing effect could play a major role in reducing friction and pressure drop. As noted earlier, small microcapsules (2 – 10 μm) suppress turbulence (Crowe et al. 1998) and have a considerable impact on pressure drop, too. The Reynolds number range is shown in each figure and is based on the apparent viscosity of the MPCM slurry at the specified mass fraction.

Convective heat transfer coefficient measurement for water

Water heat transfer tests were conducted and temperature data were collected using thermocouples and a sensitive data acquisition system as described above. The amount of power for each section was measured to determine each section's associated heat flux. Each section experimental heat transfer coefficient was calculated based on the following relation:

$$h = \frac{q''}{T_{wall} - T_{bulk}} \quad (4.4)$$

where q'' , T_{wall} , and T_{bulk} are the wall heat flux, wall temperature, and bulk fluid temperatures, respectively. The experimental convective heat transfer coefficient was analyzed and compared with the Gnielinski correlation:

$$Nu_D = \frac{\left(\frac{f}{8}\right)(Re_D - 1000)Pr}{1 + 12.7\left(\frac{f}{8}\right)^{1/2}\left(Pr^{2/3} - 1\right)} \quad (4.5)$$

where Nu_D , f , Re_D , and Pr are the Nusselt number, friction factor, Reynolds, and Prandtl numbers, respectively. The Gnielinski correlation is valid for $0.5 < Pr < 2,000$ and $3,000 < Re < 5 \times 10^6$, and takes into account the friction factor. Other correlations, including the Dittus-Boelter and Sieder and Tate correlations, are valid when the Reynolds number is greater than 10,000.

The following equation is used to determine the convective heat transfer coefficient based on the Nusselt number:

$$h = Nu_D \frac{k}{D} \quad (4.6)$$

where h , Nu_D , k , and D are the convective heat transfer coefficient, Nusselt number, fluid thermal conductivity determined at the bulk fluid temperature, and pipe diameter, respectively.

The validation experiments indicate good agreement with the Gnielinski correlation evaluated at the same conditions and fluid properties as the heat transfer experiments. Uncertainty analysis revealed that the compounded error was less than $\pm 8.0\%$. Using the Gnielinski correlation for

smooth tubing under identical conditions, fluid properties, and tubing characteristics, the enhanced tubing enhancement factor is 1.17. The enhancement factor is defined as follows:

$$Enhancement_Factor = \frac{h_{enhanced} Area_{Smooth}}{h_{smooth} Area_{smooth}} \quad (4.7)$$

where $h_{enhanced}$, h_{smooth} , and $Area_{smooth}$ are the heat transfer coefficients for enhanced tubing and smooth tubing, and the tubing cross-sectional area, respectively. The experimental heat transfer coefficient of the enhanced tubing is based on a diameter of 8 mm (smooth). However, the defined enhancement factor does not reflect the actual heat transfer area. The enhanced tubing has approximately 1.6 times the amount of surface area of smooth tubing of the same diameter.

After taking into account the enhanced tubing additional surface area, it can be concluded that the microfins or enhancements on the tubing inner surface curtail the heat transfer process but make up the difference by providing more surface area for heat transfer. This suggests that enhancements affect the momentum transfer from the wall to the bulk fluid. Zukauskas (1994) studied the impact of enhancements in detail and concluded that the height of the enhancement should only be high enough to disturb the viscous sublayer in liquids. Zukauskas (1994) defined a dimensionless roughness height, k^+ , which is defined as follows:

$$k^+ = \frac{ku_*}{\nu} \quad (4.8)$$

where k^+ , k , u_* , and ν are the dimensionless roughness, roughness height, friction velocity, and kinematic viscosity, respectively.

Previous experiments (Crowe et al. 1998) showed that k^+ should fall between 5 – 70 for improving the heat transfer rate; otherwise the enhancement could be ineffective. In the case of water at 1.76 m/sec, k^+ is about 0.25, which suggests that a higher enhancement is advisable as long as the pressure drop penalty does not increase drastically.

MPCM slurry heat transfer test

Several heat transfer experiments were conducted to determine the convective heat transfer coefficient of MPCM slurry at high and low mass frac-

tions. Temperature and power readings necessary for calculation of the heat transfer coefficient were taken when the slurry inlet temperature reached a steady-state value of approximately 1.8 °C or less. When the inlet temperature reached 1.8 °C or less, a full liquid-to-solid transformation of the phase change material was assumed. Simple energy balance calculations based on temperature, power, and flow-meter readings were performed to verify that the MPCM slurry sensible and latent heat capacities match the energy input within a margin of error of 10% or less.

Figure 4.7 and Figure 4.8 show the experimental temperature profile (temperature vs tubing length) from several heat transfer tests of MPCM slurry at 7.0% ($\pm 0.4\%$) when the slurry velocity was varied from 0.64 – 1.08 m/sec and from 1.17 – 1.50 m/sec, respectively. Also, these figures show the experimental heat capacity enhancement when assuming identical flow conditions (initial temperature and flow rate) using plain water. A 40% enhancement can be obtained when 7% of MPCM slurry is used. Figure 4.7 and Figure 4.8 also show the effect of phase change material as it absorbs energy during the melting process. The process helps maintain a lower temperature in the carrier fluid (water), which in turn allows heat transfer to occur at lower temperatures than normal.

In Figure 4.7 and Figure 4.8, the MPCM slurry temperature profile displays three primary changes in slope at approximately 5 °C that are indicative of the phase change process. Under ideal circumstances, the temperature gradient should be close to zero during phase change. However, the experimental data reveal a slope greater than zero because not all the microcapsules undergo phase change at the same time. Microcapsules closer to the tube wall undergo phase change first, affecting the slurry bulk temperature as those capsules exchange energy with the surrounding fluid and other microcapsules that have undergone only partial phase change or none at all. The shape of the temperature profile can be used to investigate the amount of particles that melt before, during, and after reaching the phase change material melting point by using energy balances on the fluid.

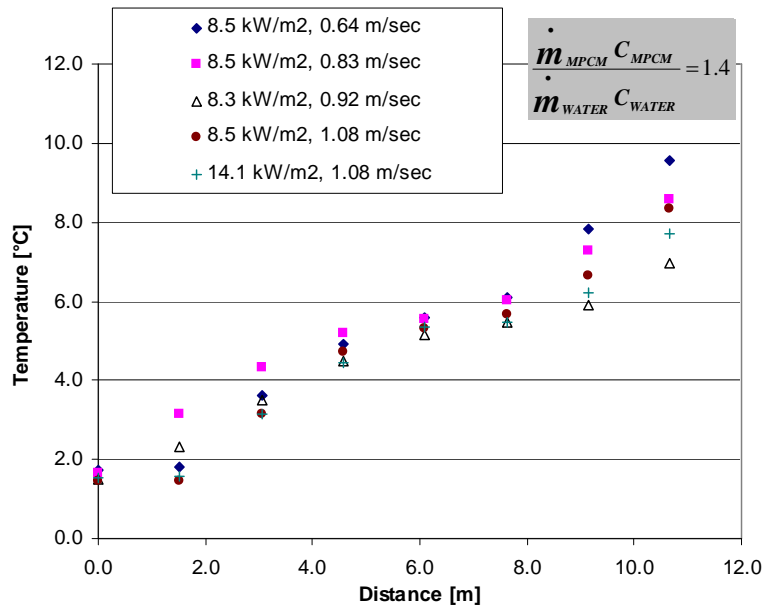


Figure 4.7. Temperature profile for MPCM slurry at 7.0%, 10.9 mm smooth tubing, Reynolds number range 3200 – 5400.

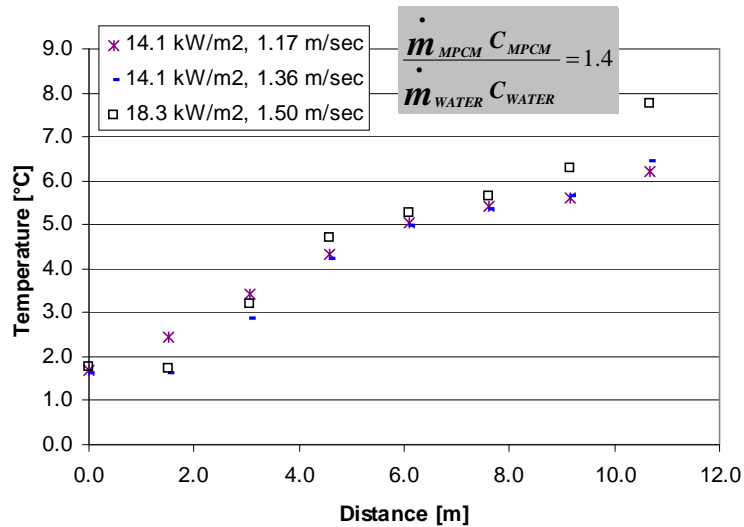


Figure 4.8. Temperature profile for MPCM slurry at 7.0%, 10.9 mm smooth tubing, Reynolds number range 5800 – 7500.

Figure 4.9 and Figure 4.10 show the experimental heat transfer coefficient for several heat transfer tests of MPCM slurry at 7.0% ($\pm 0.4\%$) within a 7% margin of error. Figure 4.7 and Figure 4.8 show how the convective heat transfer coefficient changes considerably during the phase change process, which is similar to the behavior observed by Yamagishi et al. (1999). During the phase change process, the slurry bulk temperature does not increase as fast as during the before- and after-melting segments, which is due to the additional heat capacity provided by the phase change

material. The additional heat capacity during the phase process enhances the heat transfer coefficient as shown in Figure 4.9 and Figure 4.10, and is in line with the idea that at a higher heat capacity or Prandtl number, the convective heat transfer coefficient increases accordingly (Kasza and Chen 1985). It can also be noticed that the heat transfer coefficient increases significantly with fluid velocity because momentum transfer is greater at high velocities. However, the heat transfer coefficient for MPCM slurry is lower than that for pure water at the same velocities, suggesting that the particles attenuate turbulence and momentum transfer. It is known that particle size can either enhance or suppress turbulence. Experimental data (Crowe et al. 1998) suggest that small particles such as the ones used in the project (2 – 10 μm), and whose relation to the characteristic fluid length scale is less than 0.1 (D_p/L_e), have shown considerable turbulence suppression and therefore, lower momentum transfer.

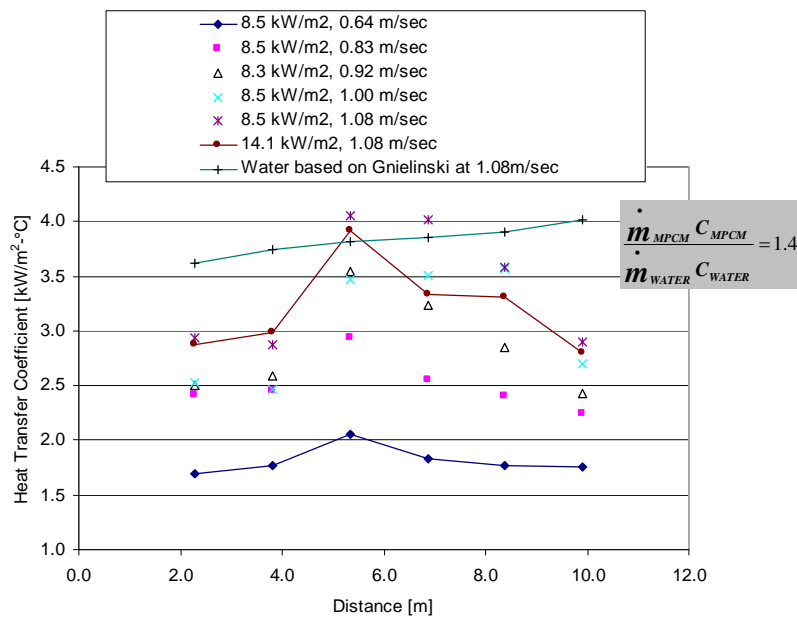


Figure 4.9. Heat transfer coefficient of MPCM slurry at 7.0%, 10.9 mm regular tubing, Reynolds number range 3200 – 5400.

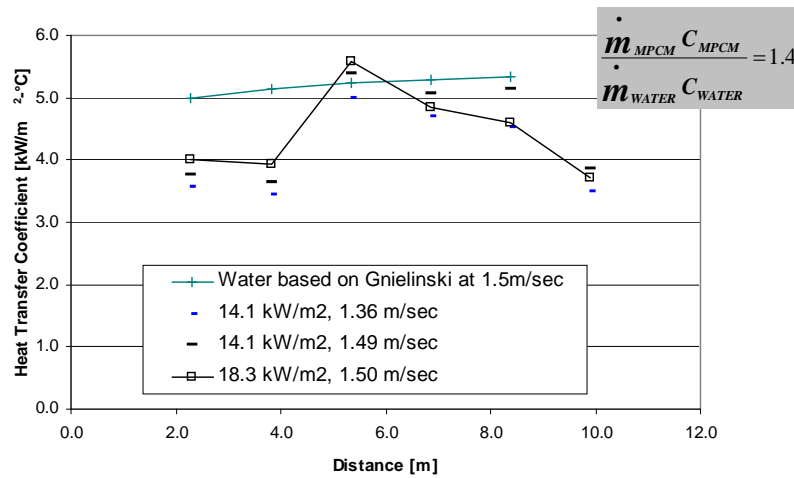


Figure 4.10. Heat transfer coefficient of MPCM slurry at 7.0%, 10.9 mm regular tubing, Reynolds number range 5800 – 7500.

Figure 4.11 shows the MPCM slurry temperature profile as a function of tubing distance at mass fractions of 16.5%, when a 10.9 mm tubing section was used. Figure 4.11 also shows that at a higher heat flux (16.3 kW/m²) and higher velocity (1.21 m/sec), the MPCM slurry exhibits noticeable changes in temperature gradient. Figure 4.12 shows the heat transfer coefficient under same conditions as in Figure 4.11. It can be noticed that the heat transfer coefficient (Figure 4.12) is much lower than that for plain water and MPCM slurry at lower mass fraction under the same conditions, which indicates that at higher mass fractions, higher apparent viscosity and lower turbulence curtails the heat transfer from the wall to the bulk fluid. On the other hand, the experimental heat capacity is considerably greater than that of water (70%) under the same conditions.

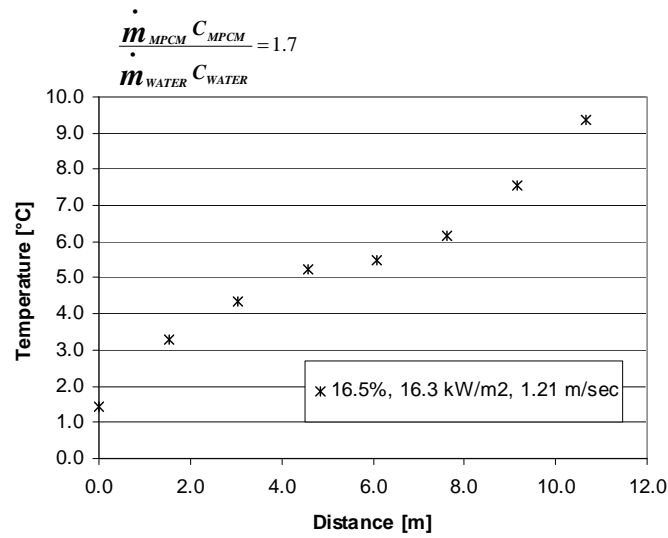


Figure 4.11. Temperature profile for MPCM slurry at 16.5%, 10.9 mm smooth tubing, Reynolds number ~ 4000.

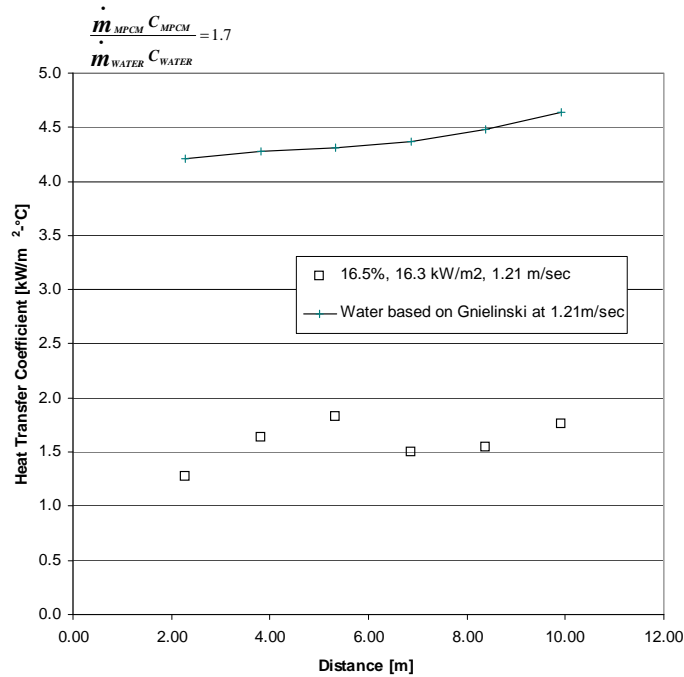


Figure 4.12. Heat transfer coefficient of MPCM slurry at 16.5%, 10.9 mm smooth tubing, Reynolds number ~ 4000.

Figure 4.13 shows the heat transfer coefficient of MPCM slurry at 7.0% mass fraction when smooth and enhanced 8 mm tubing sections were used. The experimental data may suggest that enhanced tubing does indeed improve the heat transfer process at low mass fraction, as indicated

by the enhancement factor shown in Figure 4.13. However, plain water still has a greater heat transfer coefficient under identical conditions.

$$\frac{Average_h_{MPCM_REGULAR}}{Average_h_{WATER_GNIELINSKI}} = 0.6 \qquad \frac{Average_h_{MPCM_ENHANCED}}{Average_h_{MPCM_REGULAR}} = 1.3$$

$$\frac{Average_h_{MPCM_ENHANCED}}{Average_h_{WATER_GNIELINSKI}} = 0.7$$

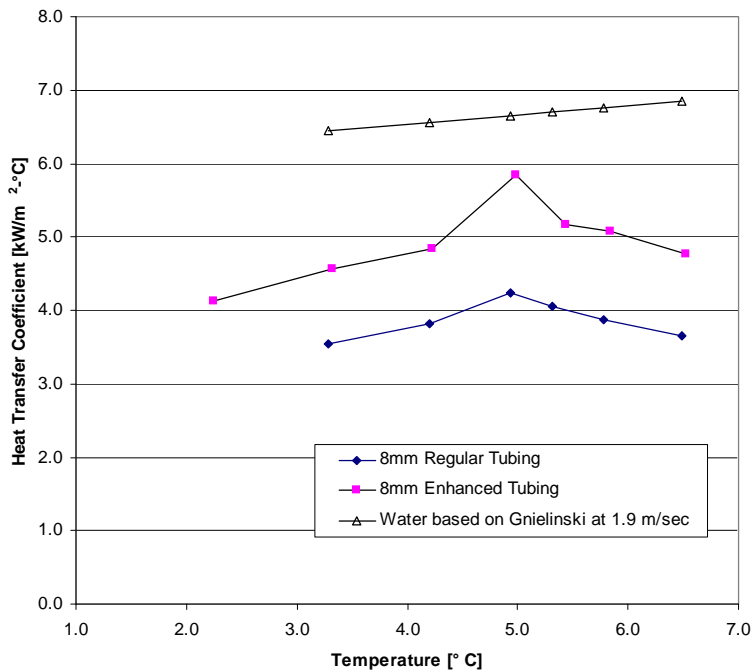


Figure 4.13. Heat transfer coefficient of MPCM slurry at 7.0%, 8 mm regular and 8 mm enhanced tubing at 1.9 m/sec, Reynolds number ~ 6900.

Figure 4.14 shows the heat transfer coefficient of MPCM slurry at 12.0% mass fraction when an 8 mm smooth (regular) tubing section was used. As in the case of the 10.9 mm tubing section, the heat transfer enhancement is 0.4, which can be attributed to lower turbulence at higher mass fractions and smaller tubing size.

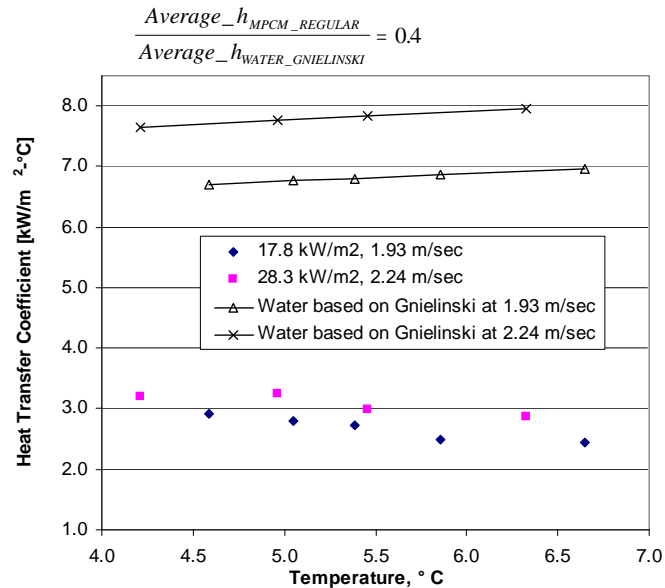


Figure 4.14. Heat transfer coefficient of MPCM slurry at 12.0%, 8 mm regular tubing at 1.9 and 2.24 m/sec, equivalent Reynolds number range 4600 – 5400

Figure 4.15 and Figure 4.16 show the heat transfer coefficient of MPCM slurry when an 8 mm enhanced tubing section is used. Figure 4.15 shows that at higher velocities and heat fluxes, the heat transfer coefficient increases considerably. The enhancement in heat transfer coefficient can be attributed to greater turbulence, which translates into greater momentum transfer from the wall to the core fluid, and also to the additional amount of heat transfer area available from the enhanced tubing. Figure 4.15 also shows that the heat transfer coefficient peaks when the slurry bulk temperature is near the melting point of n-tetradecane (the PCM). As noticed in Figure 4.9, Figure 4.10, and Figure 4.15, the phase change process has a positive impact on the heat transfer coefficient because of the additional heat capacity available from the latent heat of fusion of the PCM. Figure 4.15 also shows that the phase change process and higher mass flow rate yields significant enhancement of the heat transfer coefficient when compared with the before- and after-melting segments of the same heat transfer experiment. As in the case of single-phase fluids, the heat transfer coefficient of MPCM slurry is also a function of momentum transfer and heat capacity, as represented by the mass flow rate and increased heat capacity, respectively.

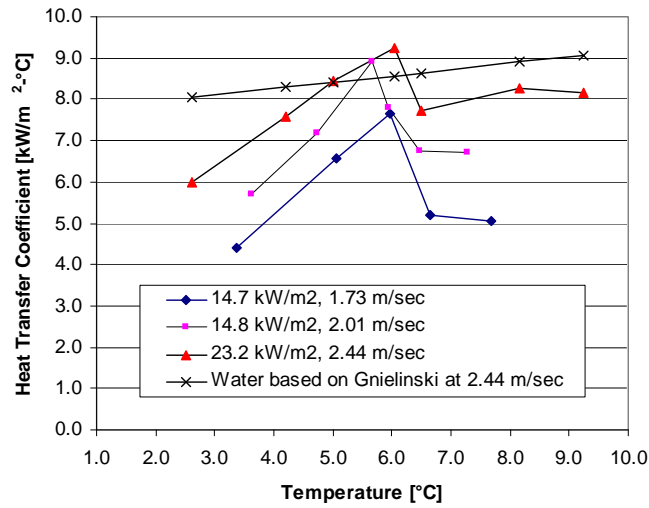


Figure 4.15. Heat transfer coefficient of MPCM slurry at 6.5%, 8 mm enhanced tubing, equivalent Reynolds number range 6300 – 8900.

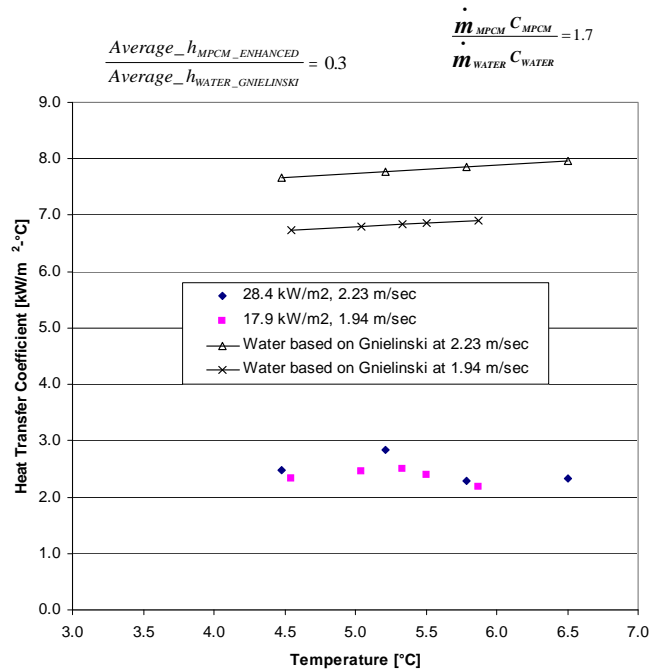


Figure 4.16. Heat transfer coefficient of MPCM slurry at 15.2%, 8 mm enhanced tubing, Equivalent Reynolds number range 3900 – 4500.

The benefits of using enhanced tubing diminish considerably at higher mass fractions, as seen in Figure 4.16. This may suggest that a larger pipe diameter and a different type of enhancement could still enhance the MPCM slurry performance at high mass fractions. Table 4.1 summarizes

the heat transfer and heat capacity enhancement factors for the tubing sections and MPCM slurry used in the experiments.

Table 4.1. Summary of percentage of particles migrating in and out of the near-wall region.

Mass Fraction %	Tubing Characteristics	Heat Flux (kW/m ²)	Slurry Velocity (m/sec)	% of Particles into Wall Region Before Bulk Fluid Reached Melting Point of PCM
7%	Smooth, 10.9 mm	8.5	0.64	3%
7%	Smooth, 10.9 mm	8.3	0.92	5%
7%	Smooth, 10.9 mm	8.5	1.08	6%
7%	Smooth, 10.9 mm	14.1	1.08	7%
7%	Smooth, 10.9 mm	14.1	1.17	6%
7%	Smooth, 10.9 mm	14.1	1.36	8%
7%	Smooth, 10.9 mm	18.3	1.5	12%
16.5%	Smooth, 10.9 mm	13.4	1.21	18%
7%	Smooth, 8 mm	13.9	1.9	14%
7%	Enhanced, 8 mm	13.9	1.9	13%
12%	Smooth, 8 mm	17.8	1.93	22%
12%	Smooth, 8 mm	28.3	2.24	27%

Another important goal of the heat transfer experiments was to determine the percentage of particles that underwent phase change before the bulk fluid reached the melting point of the PCM. This is an important part of the investigation because it reveals which conditions (flow rate, heat flux, etc.) favor such phenomenon. Simple energy balance calculations were performed based on the temperature profiles of each heat transfer experiments to determine the equivalent mass flow rate of particles that transfer from the core fluid to the viscous layer region where the wall layer fluid is at a sufficiently high temperature to cause phase change of the particles entering that region. The calculations are based on the slope of the temperature profile as well as on the heat flux, flow rate, and mass fraction used. The energy balance calculations were also used to corroborate the mass fraction tested during the experiments. Such calculations can also be used to shed light on the impact of higher heat flux (i.e., greater thermal gradient near the surface) as well as changes in flow rate (lower or higher momentum transfer from the wall to the core fluid). The uncertainty or overall error in the energy balance calculations was within $\pm 8\%$. Results from the calculations are summarized in Table 4.1.

Table 4.1 shows that higher slurry velocities increase the percentage of particles migrating into the near-wall region. The table also shows that a higher heat flux increases the migration percentage, but not as significantly as when the slurry velocity increases. A higher heat flux at similar flow rates and particle loadings results in a thicker layer of wall-region fluid with a temperature greater than the PCM's melting temperature. Significant migration can be observed when both heat flux and slurry velocities are increased considerably. This result can be explained by the increased level of turbulence and greater thermal gradient near the wall, which favors greater momentum and heat transfer.

5 Computational Modeling

Overview

In order to fully exploit the enhanced heat transfer capacity of MPCM slurry flows in any practical application, it is necessary to develop a model that accounts for all of the physics that influence the phenomenon while remaining sufficiently simple to be practical for design calculations. The present context primarily relates to the use of MPCM slurry flows in district heating and cooling applications. Correctly modeling this situation requires one to consider the effects of turbulence, convective and conductive heat transfer, two-phase flow, and energy release or gain due to phase change. Each of these problems is challenging individually, and in combination the problems are compounded. Nonetheless, it is possible to make progress by introducing several simplifications that greatly reduce the difficulty of the task. The most important of these assumptions is that the phase change process can be modeled as a source term in the statement of the conservation of energy principle. Under this assumption, one does not need to track the total enthalpy of the system or introduce any ad hoc functional forms for the specific heat as is done in the conventional treatment of flows undergoing phase change. The authors will present a new model for describing MPCM slurry flows and show that the model can reproduce experimental data. The model is intended for future use and adaptation in the design and engineering of MPCM-based systems.

Fundamental assumptions

The first and most critical simplifying assumption is that the effect of the phase change can be modeled as a volumetric source term in the energy equation. Consider a heating application in which energy is being transferred into the system, for example. When the temperature of a particular MPCM particle is below the melting temperature, phase change is not occurring and this source term is not active. When enough energy has been transferred to this fluid particle to raise its temperature to the melting point, the particle begins to change phase. This phenomenon is modeled by activating the source term to remove energy from the system. For the specific case of a straight duct heat exchanger, the analytical work of Choi et al. (1999) can be used to estimate the length of the region over which melting is taking place, as expressed in equation 5.1:

$$\frac{L_2}{L} = \frac{\rho_{hl}\phi Q_v \lambda}{\dot{Q}} \quad (5.1)$$

where L_2 is the length of the melting region, L is the length of the duct, Q_v is the volumetric flow rate, λ is the latent heat of the phase change material, ϕ is the volume fraction of the phase change material, ρ_{hl} is the density of the liquid phase change material, and \dot{Q} is the power input to the system.

It should be noted here that the Choi et al. (1999) model is one-dimensional and based on a heat transfer fluid containing PCM particles that are not encapsulated. In contrast, the slurry considered in the present study contains phase change material that has been encapsulated into gelatinous capsule with physical dimensions on the order of tens of micrometers. The principal difference between Choi et al. (1999) and the current study, then, is that the density of these microcapsules differs from that of the carrier fluid only by less than 1%. This result is also given in Yamagishi et al. (1999) for another MPCM slurry. As such, it is reasonable to assume that the MPCM particles are completely entrained in the background flow of the carrier fluid. Using these key pieces of information, the one-dimensional model of Choi et al. (1999) has been extended to two dimensions in the present work. Assuming that a particle of PCM with velocity equal to the average velocity of the flow must travel a distance of L_2 in order to fully melt, one can extract a physically relevant time scale from equation 5.1 by using the following relationship:

$$L_2 = \bar{u} * dt1 \quad (5.2)$$

$$dt1 = \frac{\rho_{MPCM} D \phi \lambda}{4\dot{q}} \quad (5.3)$$

In this expression, D is the diameter of the pipe, ρ_{MPCM} is the density of the MPCM particle, \bar{u} is the average axial velocity, and \dot{q} is the wall heat flux. The parameter $dt1$ can then be interpreted as a characteristic time for melting of a particle. Now it is necessary to make another critical assumption, which is that each MPCM particle will melt at the same rate regardless of its radial position in the pipe. This assumption is justifiable due to the enhanced radial mixing caused by the underlying turbulent flow for the majority of the pipe. It is conceivable that in a shallow region near the pipe walls where the temperature is higher than that of the bulk fluid this assumption can break down, but that factor is overlooked for purposes of

simplification. The situation is now generalized to allow for nonuniform temperature and velocity profiles in the axial and radial directions. The fluid velocity is constant along a stream line, and for the simple geometries of interest, the domain can be discretized in such a way such that the computational cells follow the stream lines in the axial direction with no distortion. It should be noted that the method being described here is not limited to straight pipes, and could be applied to other parallel flows including flow around smooth bends with a sufficiently large radius of curvature such that the streamlines remain parallel around the bend. It is also conceivable that one could consider some non-parallel flows by imposing a suitable distortion of the mesh to accommodate, for example, a change in pipe diameter. These complications are not pursued in the present study, but are left for future adaptations. Returning to the universal melting rate assumption, the distance a particle will travel along a stream line while melting, L_m , can be described by considering the local fluid velocity:

$$L_m(r) = u(r) * dt \quad (5.4)$$

A typical profile of the axial velocity as a function of the radial coordinate is shown in Figure 5.1.

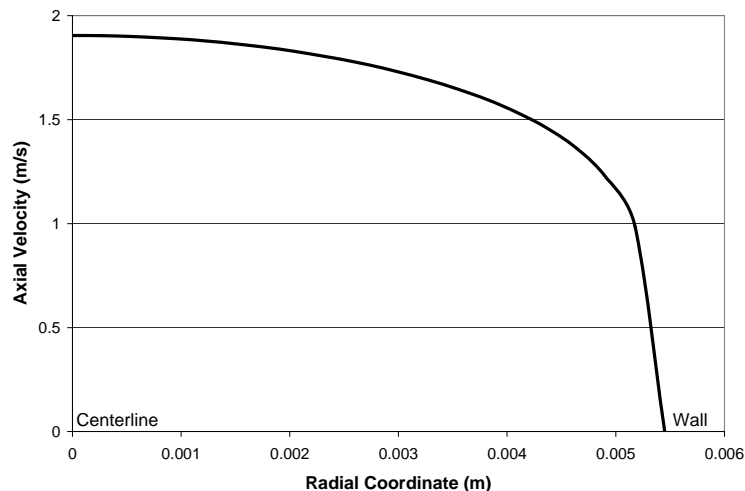


Figure 5.1. A typical mean velocity profile for turbulent pipe flow = 1.5 m/s.

It is clear that near the wall $u(r) < \bar{u}$ and thus $L_m(r) < L_2$ while away from the wall, $u(r) > \bar{u}$ and $L_m(r) > L_2$. Thus, the melting region considered by this model is more physically realistic than that considered by Choi et al. (1999), especially for moderate Reynolds number flows in which the degree of turbulent mixing is less than that of high Reynolds number flows.

Two-dimensional slices along the pipe axis of each region are shown below in Figure 5.2.

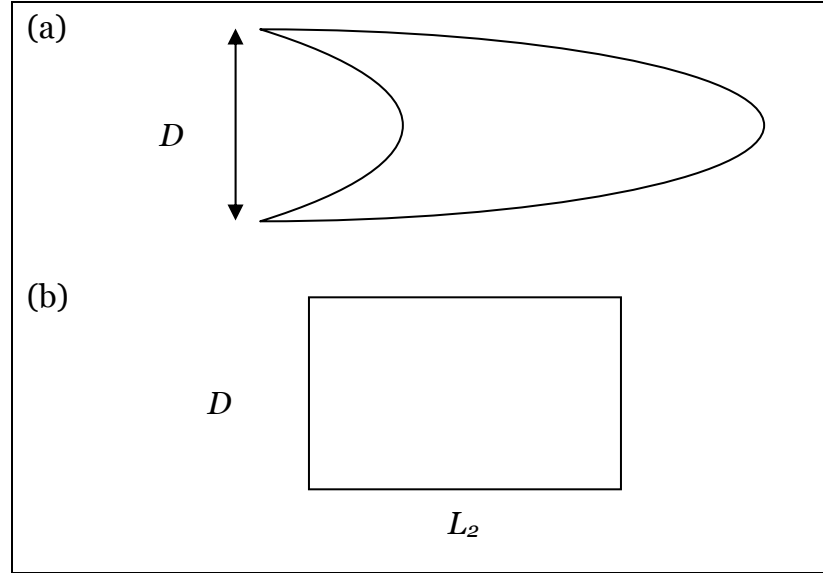


Figure 5.2. Two dimensional slices of melting region for (a) present model and (b) Choi et al (1999).

If it is now assumed that the local rate of energy transfer to the phase change process, Q_{melt} , is constant everywhere within the melting region, then the global rate of energy loss is simply $Q_{melt} * V$ where V denotes the volume of the melting region. This assumption implies that in order for the present model to be compatible with the model of Choi et al (1999), the volume of the melting region in Figure 5.2a must be equal to the volume of the region given by Figure 5.2b. One can label the curve marking the onset of melting as $l_1(r)$ and that marking the completion of melting as $l_2(r)$. Then the volume of the melting region can be found by calculating the integral in equation 5.5.

$$V_a = \int_{r=0}^{D/2} \int_{\theta=0}^{2\pi} \int_{x=l_1(r)}^{l_2(r)} dx (r dr d\theta) \quad (5.5)$$

Bearing in mind that $l_2(r) - l_1(r) = l_m(r)$, one can use equation 5.4 and the average value theorem to arrive at the following result:

$$V_a = dt \int \frac{\pi D^2 \bar{u}}{4} = V_b \quad (5.6)$$

The next task is to define the source term in the energy equation that models the local rate of energy transfer to the melting process per unit volume,

Q_{melt} . The total latent heat per unit volume is simply the product of the effective latent heat of the MPCM particle, the local volume fraction of MPCM particles, and density of the particles. Then to be dimensionally correct, one must introduce a second characteristic time scale into the model, dt_2 , which yields the following relationship for Q_{melt} .

$$Q_{melt} = \frac{\lambda \phi \rho_{MPCM}}{dt_2} \quad (5.7)$$

The total amount of energy removed from the melting region per unit time is then found using equations 5.6 and 5.7 as follows:

$$Q_{total} = \frac{dt_1}{dt_2} \rho_{MPCM} Q_v \phi \lambda \quad (5.8)$$

A simple control volume analysis shows that Q_{total} must obey the following relationship in the absence of any other sources or sinks of energy:

$$Q_{total} = \rho_{MPCM} Q_v \phi \lambda \quad (5.9)$$

This relationship implies that in the ideal case, $dt_1 = dt_2$. This result should not be a surprise since the relationship derived in equation 5.3 shows that dt_1 should depend only on the magnitude of the heat flux into the pipe. This implies that dt_1 can be thought of as a characteristic time for the phase change in addition to the kinematic interpretation initially assigned to it. Because the problem deals with real flows at finite Reynold's numbers, the independence of dt_1 and dt_2 will be retained in order to have more flexibility in the model. As such, one can consider the ratio dt_1/dt_2 as a rough measure of how closely the flow approximates the ideal turbulent flow paradigm.

Implementation

For the present work, the phase change model developed above was used in conjunction with a commercial computational fluid dynamics (CFD) package. The flow considered was the turbulent flow of a mixture of two incompressible phases through a straight, axisymmetric pipe with uniform heat flux along the pipe wall. In order to deal with the turbulence, the Reynolds Averaged Navier Stokes (RANS) equations are considered along with an appropriate turbulence model described below. The existence of the secondary phase adds an extra layer of complexity to these equations.

The secondary phase is accounted for by defining mixture-averaged quantities for the thermodynamic variables and by introducing a new transport equation for the volume fraction of the secondary phase. Equations 5.10 and 5.11 describe how mixture-averaging is performed for the density, ρ (or any other thermodynamic quantity) and the velocity components, respectively. The subscript “m” in these equations signifies a mixture-averaged quantity.

$$\rho_m = \sum_{k=1}^n \alpha_k \rho_k \quad (5.10)$$

$$\mathbf{U}_m = \frac{\sum_{k=1}^n \alpha_k \rho_k \mathbf{U}_k}{\rho_m} \quad (5.11)$$

The governing equations for this two-phase flow are then given by:

$$\frac{\partial}{\partial t}(\rho_m) + \nabla \cdot (\rho_m \mathbf{U}_m) = 0 \quad (5.12)$$

$$\frac{\partial}{\partial t}(\rho_m \mathbf{U}_m) + \nabla \cdot (\rho_m \mathbf{U}_m \mathbf{U}_m) = -\nabla p + \nabla \cdot [\mu_m (\nabla \mathbf{U}_m + \nabla \mathbf{U}_m^T)] - \rho_m \langle \mathbf{u}_m \mathbf{u}_m \rangle \quad (5.13)$$

$$\frac{\partial}{\partial t} \sum_{k=1}^n (\alpha_k \rho_k E_k) + \nabla \cdot \sum_{k=1}^n [\alpha_k \mathbf{U}_k (\rho_k E_k + p)] = \nabla \cdot (\lambda_{eff} \nabla T) + S_E \quad (5.14)$$

$$\frac{\partial}{\partial t}(\alpha_k \rho_k) + \nabla \cdot (\alpha_k \rho_k \mathbf{U}_m) = 0 \quad (5.15)$$

where \mathbf{U} is the mean velocity vector, \mathbf{u} is the turbulent velocity fluctuation vector, p is the pressure, μ is the absolute viscosity, α is the volume fraction of the secondary phase, λ is the effective thermal conductivity, E is the total energy, and S_E is a source term.

The effects of the turbulence are modeled using the standard k- ϵ turbulence model. This involves defining a turbulent viscosity, ν_T , and solving transport equations for the turbulent kinetic energy, k , and the turbulent dissipation rate, ϵ . The relevant equations and model constants used to close the RANS equations are listed below:

$$\langle \mathbf{u}_m \mathbf{u}_m \rangle = \frac{2}{3} k \mathbf{I} - \nu_T (\nabla \mathbf{U}_m + \nabla \mathbf{U}_m^T) \quad (5.16)$$

$$\nu_T = \frac{C_\mu k^2}{\varepsilon} \quad (5.17)$$

$$\lambda_{eff} = \lambda + \frac{\rho_m c_p \nu_T}{Pr_T} \quad (5.18)$$

$$\frac{\partial}{\partial t} (\rho_m k) + \nabla \cdot (\rho_m \mathbf{U}_m k) = \nabla \cdot \left[\rho_m \frac{\nu_T}{\sigma_k} \nabla k \right] + \rho_m \langle \mathbf{u}_m \mathbf{u}_m \rangle \nabla \mathbf{U} - \rho_m \varepsilon \quad (5.19)$$

$$\frac{\partial}{\partial t} (\rho_m \varepsilon) + \nabla \cdot (\rho_m \mathbf{U}_m \varepsilon) = \nabla \cdot \left[\rho_m \frac{\nu_T}{\sigma_\varepsilon} \nabla \varepsilon \right] + C_{\varepsilon 1} \frac{\rho_m \langle \mathbf{u}_m \mathbf{u}_m \rangle \nabla \mathbf{U}_m \varepsilon}{k} - C_{\varepsilon 2} \frac{\rho_m \varepsilon^2}{k} \quad (5.20)$$

$$Pr_T = 0.85 \quad C_{\varepsilon 1} = 1.44 \quad C_{\varepsilon 2} = 1.92 \quad C_\mu = 0.09 \quad \sigma_k = 1.0 \quad \sigma_\varepsilon = 1.3 \quad (5.21)$$

The geometry considered in this study is that of a straight, axisymmetric pipe as shown in Figure 5.3.

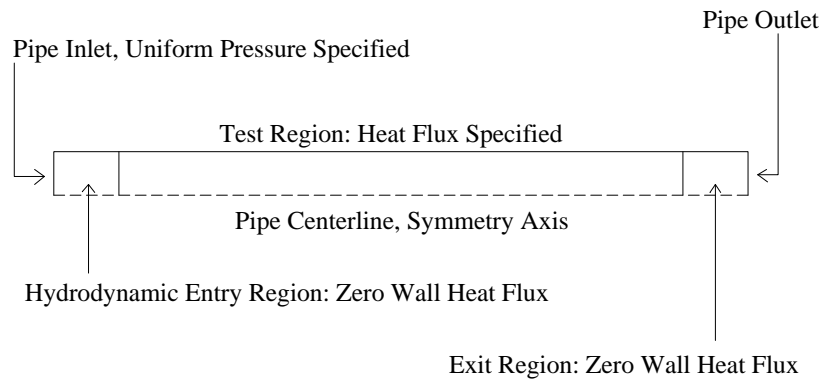


Figure 5.3. Model geometry and boundary conditions (not drawn to scale).

The model is an idealization of the experimental apparatus described in great detail by Alvarado (2004), and the item of interest here is only the heating portion of the complete heat transfer loop. Consider a pipe segment of finite length divided conceptually into three regions. The region nearest the inlet, designated the hydrodynamic entry region, is perfectly insulated (zero wall heat flux) and serves to convert an inlet plug flow into a fully developed turbulent Poiseuille flow. The second region, designated

the test region, is supplied with a constant uniform wall heat flux. The final region, designated the exit region, simply serves as a perfectly insulated buffer region leading to the outlet of the pipe. Its main purpose is to ease the transition numerically from the uniform heat-flux wall to ambient outlet conditions.

To close this section, the conditions at each of the boundaries must be specified. As indicated in Figure 5.3, the pipe centerline is modeled as a perfect symmetry axis and thus the flow does not vary in the azimuthal direction. The turbulence quantities, k and ε , are determined at the inlet by specifying the turbulence intensity, I , and the hydraulic diameter of the pipe, L , and applying the following set of equations:

$$I \equiv \frac{u}{U_{ave}} \quad (5.22)$$

$$l = 0.07L \quad (5.23)$$

$$k = \frac{3}{2}(U_{ave}I)^2 \quad (5.24)$$

$$\varepsilon = C_{\mu}^{3/4} \frac{k^{3/2}}{l} \quad (5.25)$$

Here, U_{ave} is the average mean velocity at the inlet and l is the turbulent length scale. In all of the calculations that will be presented, a turbulence intensity of 0.06 was used, and the hydraulic diameter was set to equal the diameter of the pipe. Backflow turbulence conditions are specified at the pipe outlet that are equal to those specified at the inflow. This is necessary in case the flow should reverse direction at any point along the outflow boundary. At the pipe wall, the turbulence is treated using standard wall functions. The interested reader is referred to Launder and Spalding (1974) for details on this procedure. The total pressure, temperature, flow direction, and volume fraction of the secondary phase are specified at the inlet, while at the outlet only the pressure (taken to be zero) is specified, and values for all other variables are extrapolated from the interior. No slip boundary conditions are specified at the wall in addition to the heat flux boundary conditions described earlier. The steady-state versions of the governing equations are solved using the finite volume technique. An initial estimation is made for the flow variables, and the solution is iterated upon until a converged solution is achieved.

It is necessary here to make a few remarks about the thermal properties used in these simulations. While the analytical model of Choi et al. (1999) was developed and tested for slurries of nonencapsulated PCMs that have well defined thermal properties, the present study is concerned with PCMs that have been encapsulated. The encapsulation process adds a layer of complexity to slurry mixture and has a significant effect on the thermal properties of the PCMs. In principle it is possible to calculate the composite thermal properties of the MPCM particles if one knows the proper physical dimensions and the thermal properties of the constituent materials. This exercise is likely to yield values that are close to the true values of the slurry, but one must keep in mind that the manufacturing process is imperfect and deviations in thermal properties could occur within the same batch or across batches during production. It is then advisable to use experimental data to build proper thermal property correlations to use as input for the proposed model. This is the approach taken by the authors in this study.

Results

This section examines the ability of this phase change model to reproduce selected experimental results obtained by Yamagishi et. al. (1999) and Alvarado (2004).

Figure 5.4 shows the centerline temperature profile extracted from the simulation plotted with Yamagishi's experimental data for the case of a water/octadecane MPCM mixture with the following conditions: $\dot{q} = 19.984 \text{ kW/m}^2$, $\bar{u} = 1.25 \text{ m/s}$, and $\alpha = 0.12$. The Reynolds number of this flow is defined as follows:

$$\text{Re} = \frac{\rho \bar{u} D}{\mu} \quad (5.26)$$

where ρ and μ are the density and dynamic viscosity of the slurry, respectively, and \bar{u} and D are the average velocity and pipe diameter respectively. The Reynolds number varies from 7360 to 8650 due to variations in slurry viscosity with temperature.

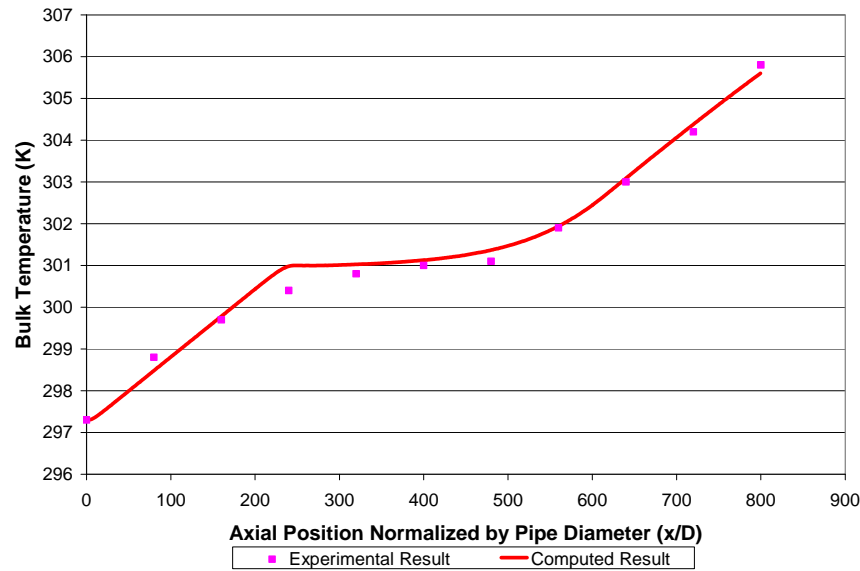


Figure 5.4. Computed and experimental (Yamagishi et al. 1999) bulk temperature profiles along pipe axis; $\dot{q} = 19.984 \text{ kW/m}^2$, $\bar{u} = 1.25 \text{ m/s}$, and $\alpha = 0.12$.

The result shown in Figure 5.4 was generated using $dt1 = 2.23$ and $dt2 = 2.23$. In this plot, along with all subsequent plots, the value of $dt1$ is calculated according to equation 3. The value of $dt2$ was varied in the vicinity of $dt1$ until the computed solution closely followed the experimental data. It is possible then to a posteriori check the ratio $dt1/dt2$, which completely describes the ratio of the total amount of energy actually removed from the system to the total amount that should be removed under ideal conditions. In the case considered here, $dt1/dt2 = 1.0$ as the real flow corresponds well to an ideal turbulent flow. However, a potential pitfall encountered when using turbulence models is discussed below.

The first case of interest in Alvarado (2004) is similar to Yamagishi's experiment described above. It is a high Reynolds number ($Re = 5870 - 7270$) flow with a high wall heating rate but a lower particle volume fraction. Under these conditions, one would expect the flow to closely exhibit the characteristics of the ideally turbulent flow paradigm, namely that setting $dt1 = dt2$ should yield results that closely approximate the experimental data. Figure 5.5 confirms this expectation. Note that in both Figure 5.4 and Figure 5.5, the temperature in the vicinity of the location of the onset of melting is overpredicted by the model. This result can be explained by the concept of supercooling. It is well known that MPCM particles exhibit a difference of several kelvins between their melting and freezing temperatures. The phase change model implies that particles melt and freeze instantaneously upon crossing a common temperature threshold. The re-

solidification process releases energy back to the system resulting in a higher temperature than observed experimentally where the particles do not resolidify.

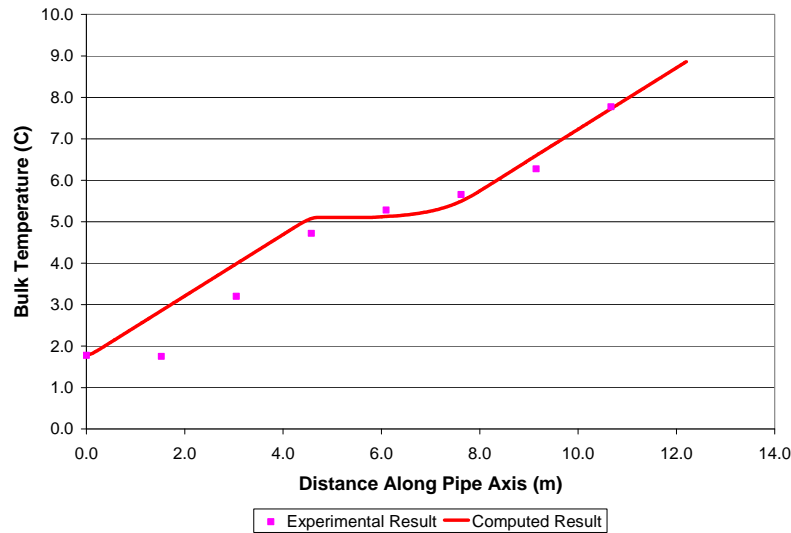


Figure 5.5. Computed and experimental (Alvarado 2004) bulk temperature profiles along pipe axis; $\dot{q} = 18.3 \text{ kW/m}^2$, $\bar{u} = 1.50 \text{ m/s}$, and $\alpha = 0.07$.

Now consider a lower Reynolds number ($Re = 3600 - 4250$) flow coupled with a lower heating rate. It is unlikely that the ideal turbulent model can faithfully reproduce the experimental data. This case is shown in Figure 5.6. Note that the ideal model, $dt_1 = dt_2$, yields results that underpredict the bulk temperature by over 1°C . In order to approach the experimental data, the value of dt_2 must be substantially increased. That change serves to decrease the ratio dt_1/dt_2 and effectively limits the amount of energy removed from the system. In the experimental configuration it is unlikely that full phase change occurred throughout the system. The calculations suggest that only approximately 60% of the available phase change material has actually changed phase despite the apparent rise in the bulk temperature above the melting temperature. The most likely reason for this discrepancy is that the real flow consists of a laminar core region where the particles do not have sufficient time to melt. Yamagishi et al. (1999) discuss this topic in more detail. It is noted, however, that the presence of the small-diameter particles ($2 - 10 \mu\text{m}$) possibly serves to suppress turbulent fluctuations in the flow. Abbas and Crow (1987) show that turbulence is suppressed in slurry flows with a d_p/L_e ratio lower than 0.001 where d_p is the particle diameter and L_e is the fluid length scale, interpreted to be the diameter of the pipe in this geometry. For the experimental conditions

of Yamagishi et al. (1999) this ratio is approximately 0.001, supporting the hypothesis that this flow is not fully turbulent.

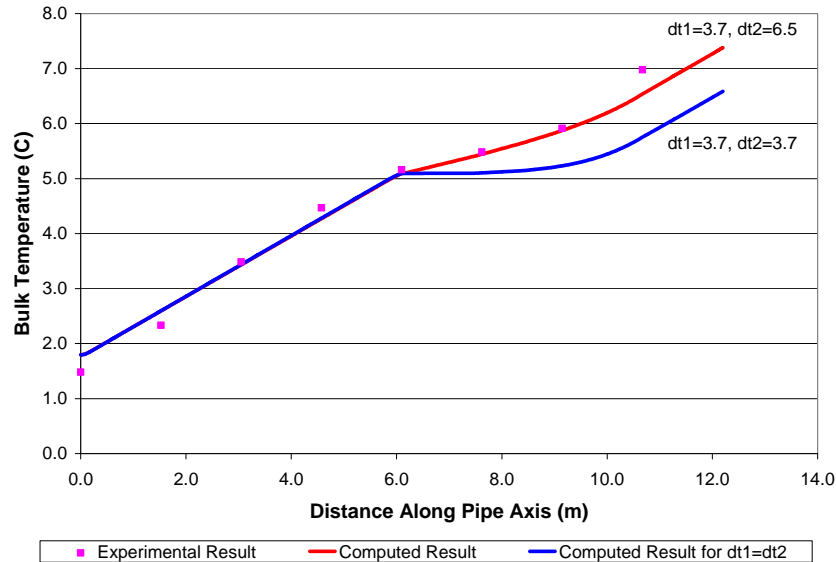


Figure 5.6. Computed and experimental (Alvarado 2004) bulk temperature profiles along pipe axis; $\ddot{q} = 8.3 \text{ kW/m}^2$, $\bar{u} = 0.83 \text{ m/s}$, and $\alpha = 0.07$.

Because the purpose of a heat exchanger is to transfer thermal energy between an intervening fluid and the external environment, it is of great interest to be able to quantify the energy exchange. In this context, a heat transfer coefficient is defined according to the following equation:

$$h = \frac{\ddot{q}}{T_{wall} - T^*} \quad (5.27)$$

where T_{wall} is the temperature at the inner surface of the pipe wall and T^* is the average (or bulk) temperature. Figure 5.7 shows the heat transfer coefficient as a function of axial position along the heat exchanger that results from equation 5.27 for the experiment discussed previously in Figure 5.5. It can be seen that the computational model overpredicts the heat transfer coefficient. However, there is at least some degree of qualitative agreement between the two curves, most notably the presence of a peak in the phase change region. Yamagishi et al. (1999) argue that the sharp increase in h begins when particles in the near-wall region begin to melt before those in the core region, as solid particles randomly migrate into this layer to melt and subsequently reduce the wall temperature. A subsequent decrease in h begins when the core region reaches the melting temperature and the particles therein begin to melt. Two observations can be made

from Figure 5.7 and Figure 5.8. The first is that the predicted magnitude of the peak in h is much smaller than that discovered experimentally. Second is that the location of the predicted peak is shifted downstream of the experimental peak. Both of these observations can be explained by examining the turbulence model and computational grid used in this exercise. As mentioned above, the k - ϵ turbulence model was chosen as a simple yet robust model of turbulent pipe flow. In order to apply this model correctly, the computational grid must be sufficiently coarse so that the first grid point lies within the log-law region, $y^+ \sim 30$, where y^+ is a nondimensional distance from the wall scaled by the wall shear stress and kinematic viscosity. The point to be made is that the thermal boundary layer cannot be resolved using this turbulence model. The wall temperature, T_{wall} , is calculated using a similar log-law relationship. Problems are encountered because the implementation of the phase change model begins when temperature at the computational cell center reaches the melting temperature. The lack of resolution of the thermal boundary layer then effectively shifts the onset of melting in the computational domain downstream of that observed experimentally. If one increases the near-wall grid resolution, the log-law relationship is no longer valid, and serious problems result. Figure 5.9 shows the results of such an increase in resolution. The data presented are the variations in the local heat transfer coefficient for Yamagishi's (1999) experiment described above in Figure 5.4. It can be seen that the predicted heat transfer coefficient is too large by a factor of approximately 4. The discrepancy between the computed and experimental results is much more pronounced for this case. It is noted that the predicted bulk temperature profiles agree quite well with the experimental data (Figure 5.4) in spite of the problems encountered in the near-wall region. The point to be understood is that one must carefully consider both the turbulence model and the near-wall computational grid in order to generate useful information.

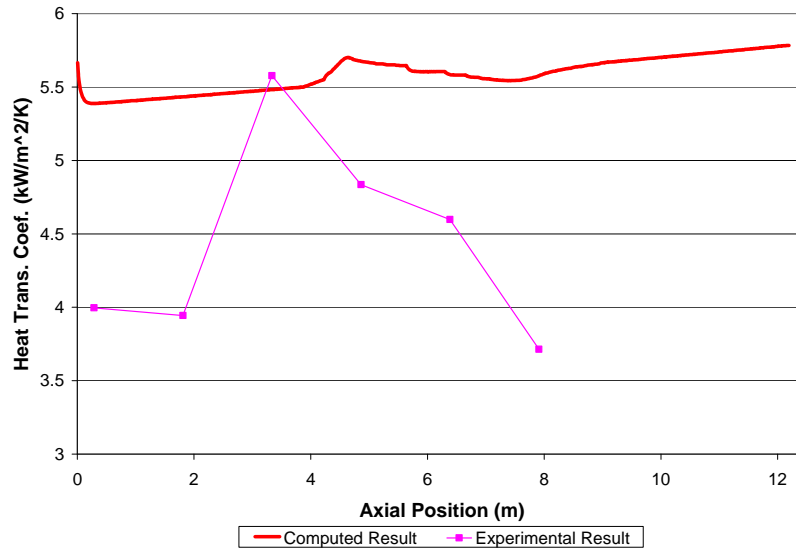


Figure 5.7. Computed and experimental (Alvarado 2004) heat transfer coefficient profiles along length of heat exchanger; $\ddot{q} = 18.3 \text{ kW/m}^2$, $\bar{u} = 1.50 \text{ m/s}$, and $\alpha = 0.07$.

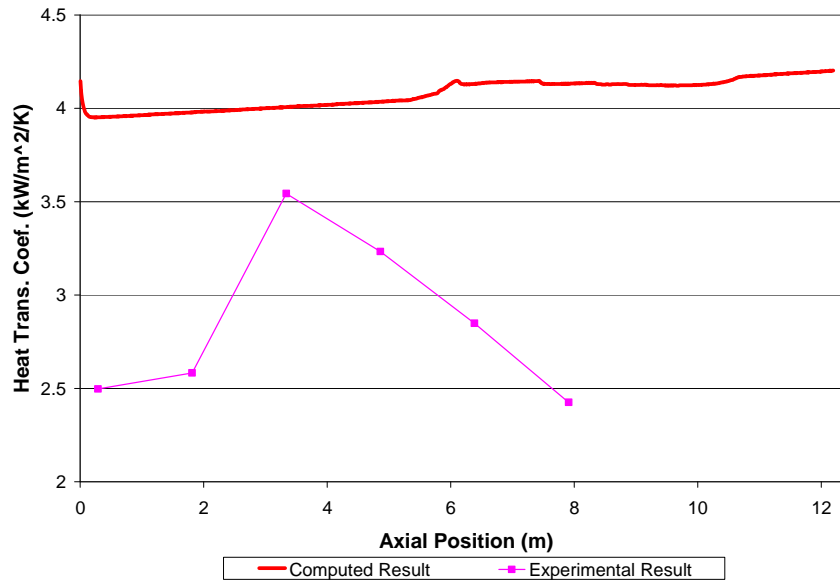


Figure 5.8. Computed and experimental (Alvarado 2004) heat transfer coefficient profiles along length of heat exchanger; $\ddot{q} = 8.3 \text{ kW/m}^2$, $\bar{u} = 0.92 \text{ m/s}$, and $\alpha = 0.07$.

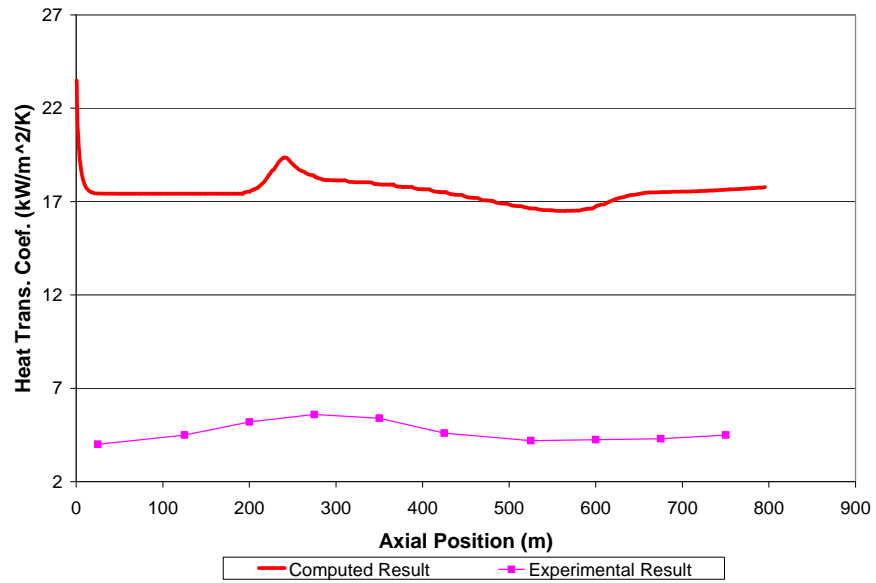


Figure 5.9. Computed and experimental (Yamagishi et al. 1999) heat transfer coefficient profiles along length of heat exchanger; $\ddot{q} = 19.984 \text{ kW/m}^2$, $\bar{u} = 1.25 \text{ m/s}$, and $\alpha = 0.07$.

6 Conclusion and Recommendations

Conclusions

The experimental data presented in this report show that MPCM slurry can provide considerable heat capacity enhancement for a thermal transfer system. Specifically, the following conclusions are drawn:

- Thermal characterization of MPCM slurry by using DSC reveals that supercooling of the PCM can be suppressed significantly by incorporating the right amount and type of nucleating agent.
- MPCM slurries exhibit a Newtonian-like behavior at mass fractions below 17.7%, and the relative viscosity is independent of temperature.
- Microcapsules become durable and impact-resistant when smaller than 10 μm .
- Pressure drop experiments revealed a possible drag-reducing effect from the use of microcapsules that should be investigated further.
- Heat transfer experiments showed that the heat capacity enhancement provided by MPCMs is considerable even at low mass fractions.
- MPCM slurry heat transfer coefficients are typically lower than that of water under the same flow conditions, even when enhanced-surface tubing was used.
- The heat transfer coefficient increases considerably during the phase change process.
- Enhanced surface tubing is more advantageous at low mass fraction than at a high mass fraction.
- Particle migration before, during, and after the bulk fluid reaches the PCM melting point is affected by slurry velocity more significantly than by heat flux. High heat fluxes also affect the migration rate of particles into the near-wall region.

MPCM slurries have the potential to become effective heat transfer fluids in district cooling applications. The enhanced heat capacity of MPCM slurries can increase a system's thermal capacity even at low mass fraction.

This work also represents a first step in coupling a phase change model to flows of an incompressible, two-phase fluid. It has been shown that the model can successfully predict the bulk temperature profile of a fluid along the heat exchanger for flows with a high degree of turbulence without modification. Low Reynolds number flows can also be treated by modify-

ing the rate at which energy is removed from the system during the melting process. In principle, one could develop an empirical relationship between the ratio dt_1/dt_2 and the Reynolds number for these types of flows. Equipped with such information, this model could be used to design heat exchangers to be used with MPCM slurries in lieu of resource-intensive experimentation.

Recommendations

This study raised several issues that should be explored in future work:

- The supercooling effect needs to be modeled in order to more accurately predict the thermal behavior of MPCM slurry before it reaches the melting region. This will become particularly important as one tries to model a closed-loop heat exchanger.
- Better near-wall treatments need to be developed in order to more accurately predict the onset of melting and to model the actual amount of heat transfer taking place within the heat exchanger.
- A wider range of turbulence models should be considered in attempts to more faithfully reproduce the behavior of the particles within the thermal boundary layer.
- More durable capsule materials should be developed to resist harsh environments.
- More types of enhanced pipe surfaces that may enhance MPCM slurry heat transfer coefficient should be identified and tested.

References

- Abbas M.A., and C.T. Crowe. 1987. Experimental study of the flow properties of a homogeneous slurry near transitional Reynolds numbers. *Int. J. Multiphase Flows* 13, 357.
- Alvarado, J. 2004. *Thermal performance of microencapsulated phase change material slurry*. Ph.D thesis. Urbana, IL: University of Illinois at Urbana-Champaign.
- American Society of Heating, Refrigerating, and Air-Conditioning Engineers (ASHRAE). *ASHRAE Handbook Fundamentals*, chap 38. Atlanta, GA: American Society of Heating, Refrigerating, and Air-Conditioning Engineers.
- Charsley, E.L., and S.B. Warrington. 1992. *Thermal analysis: Techniques and applications*. Cambridge, England: Thomas Graham House.
- Chen, K., and M. M. Chen. 1987. An analytical and experimental investigation of the convective heat transfer of phase-transition slurry flow. *Proceedings of the International Symposium on Multiphase Flow*, Eds. Z. Q. Fan and C. T. Crowe. ISBN 7 - 308 - 00039 - 7. Zhejiang University Press: Hanzhou, China.
- Cho, K., and S.H. Choi. 2000. Thermal characteristics of paraffin in a spherical capsule during freezing and melting processes. *International Journal of Heat and Mass Transfer* 43(17), 3183-3196.
- Choi, E. May 1993. *Forced convection heat transfer with water and phase-change material slurries: Turbulent flow in circular tube*. Ph.D thesis. Philadelphia, PA: Drexel University.
- Choi, E., and Y.I. Cho. 1995. Local friction and heat transfer behavior of water in a turbulent pipe flow with a large heat flux at the wall. *Journal of Heat Transfer* 117, 283-288.
- Choi, E., Y.I. Cho, and H.G. Lorsch. 1991. Effects of emulsifier on particle size of a phase change material in a mixture with water. *International Communications in Heat Mass Transfer* 18, 759-766.
- Choi, E., Y.I. Cho, and H.G. Lorsch. 1992. Thermal analysis of the mixture of laboratory and commercial grades hexadecane and tetradecane. *International Communications in Heat Mass Transfer* 19, 1-15.
- Choi, E., Y.I. Cho, and H.G. Lorsch. 1994. Forced convection heat transfer with phase-change-material slurries: Turbulent flow in a circular tube. *International Journal of Heat and Mass Transfer* 37(2), 207-215.
- Crowe, C., M. Sommerfeld, and Y. Tsuji. 1998. *Multiphase flows with droplets and particles*. Boca Raton, FL: CRC Press.
- Durmus, A., A. Durmus, and M. Esen. 2002. Investigation of heat transfer and pressure drop in a concentric heat exchanger with snail entrance. *Applied Thermal Engineering* 22, 321-332.

- Fossa, M., and L.A. Tagliafico. 1995. Experimental heat transfer of drag-reducing polymer solutions in enhanced surface heat exchangers. *Experimental Thermal and Fluid Science* 10, 221-228.
- Goel, M., S.K. Roy, and S. Sengupta. 1994. Laminar forced convection heat transfer in microcapsulated phase change material suspensions. *International Journal of Heat Mass Transfer* 37(4), 593-604.
- Hatakeyama, T., and F. X. Quinn. 1994. *Thermal Analysis: Fundamentals and Applications to Polymer Science*. New York, NY: John Wiley & Sons.
- Hetsroni, G. 1989. Particles-turbulence interaction. *International Journal of Multiphase Flow* 15(5): 735-746.
- Kasza, K.E., and M.M. Chen. 1985. Improvement of the performance of solar energy waste heat utilization systems by using phase-change slurry as an enhanced heat transfer storage fluid. *Journal of Solar Energy Engineering* 107, 229-236.
- Kostic, M. 1994. On turbulent drag and heat transfer reduction phenomena and laminar heat transfer enhancement in non-circular duct flow of certain non-Newtonian fluids. *International Journal of Heat and Mass Transfer* 37 (suppl. 1), 133-147.
- Liao, Q., and M. D. Xin 2000. Augmentation of convective heat transfer inside tubes with three-dimensional internal extended surfaces and twisted-tape inserts. *Chemical Engineering Journal* 78, 95-105.
- Liu, K. V., U.S. Choi, and K.E. Kasza. 1998. *Measurements of pressure drop and heat transfer in turbulent pipe flows of particulate slurries*. Argonne, IL: Argonne National Laboratory.
- Ohtsubo, T., S. Tsuda, and K. Tsuji. 1991. A study of the physical strength of fenitrothion microcapsules. *Polymer* 32(13): 2395-2399.
- Roy, S. K. and B. L. Avanic. 1997. Laminar forced convection heat transfer with phase change material emulsions. *International Communications in Heat Mass Transfer* 24(5): 653-662.
- Roy, S. K. and S. Sengupta. 1991. An evaluation of phase change microcapsules for use in enhanced heat transfer fluids. *International Communications in Heat Mass Transfer* 18: 495-507.
- Speyer, R.F. 1994. *Thermal Analysis of Materials*. New York, NY: Marcel Dekker, Inc.
- Thomas, David G. 1965. Transport Characteristics of Suspensions: VIII. A note on the viscosity of Newtonian suspensions of uniform spherical particles. *Journal of Colloid Science* 20: 267-277.
- Vand, V. 1948. Viscosity of solutions and suspensions. II: Experimental determination of the viscosity-concentration function of spherical suspensions. *Journal of Physical Colloid Chemistry* 52: 300-321.
- Winters, P.J. 1991. Phase two laboratory testing of direct freeze ice slurry district cooling. Final report, Department of Energy contract no. DE-FG01-88CE26559. Washington, DC: U.S. Department of Energy.

- Yamagishi, Y., T. Sugeno, T. Ishige, H. Takeuchi, and A.T. Pyatenko. 1996. An evaluation of microencapsulated PCM for use in cold energy transportation medium. *Proceedings of the Intersociety of Energy Conversion Engineering Conference*, 2077-2083. New York, NY: Institute of Electrical and Electronics Engineers (IEEE).
- Yamagishi, Y., H. Takeuchi, A.T. Pyatenko and N. Kayukawa. 1999. Characteristics of MPCM slurry as a heat transfer fluid. *AIChE Journal*, 45(4), 696-707.
- Zukauskas, A. 1994. Enhancement of forced convection heat transfer in viscous fluid flows. *International Journal of Heat and Mass Transfer* 37 (suppl.1), 207-212.

Appendix: Effects of Temperature and Volume Fraction on Slurry Viscosity

Introduction

During the course of the work detailed in this report, much attention was paid to the model of viscosity and its determining parameters. While the Vand model incorporated the volume fraction only, it appeared that temperature may also have a significant effect. This appendix outlines the steps taken to achieve a model, including both volume fraction and temperature effects.

Current viscosity approximations

Figure A1 shows the comparison of viscosity measurements using the Thomas Correlation (Thomas 1965) and the method of Yamagishi et al (1996). At low volume fractions, the viscosity measurements are nearly the same, but they gradually diverge at higher volume fractions.

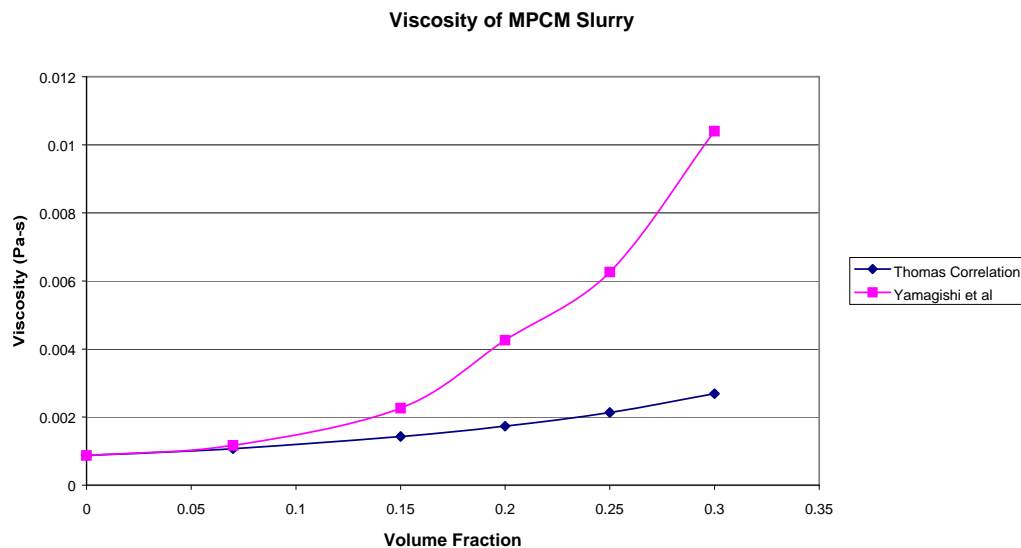


Figure A1. Viscosity vs volume fraction calculated using Thomas Correlation and Yamagishi et al. (1996).

New viscosity function approximation

The desire for $\mu = A + B + C$ to approximate a viscosity function, where A, B, and C are the different parameters effecting the viscosity, is simple: it

amounts to a three-dimensional function (one dependent and two independent variables) where there is a two-dimensional function for the single dependent variable versus each of the two independent variables separately. In the three-dimensional space of the desired function, each function is a two-dimensional plane, so the temperature function is simply the plane orthogonal to the ϕ axis.

As long as it is assumed that the function for viscosity versus temperature applies at each “volume-fraction plane,” then one can simply replace the μ_r with the viscosity-versus-temperature function:

$$\mu = \mu(\phi, T) = (1 - \phi - C\phi^2)^D A e^{-BT}, \quad (\text{A1})$$

where ϕ is the volume fraction, T is the temperature, and A , B , C , and D are the unknown constants. This expression reduces to the correct effect for $\phi = 0$ and for any reference temperature assuming, again, that the temperature model applies at all volume fractions. It also assumes that the temperature effects are entirely independent of the volume fraction effects, with no “cross-product” effects that scale like volume fraction to a power of temperature. Figure A2 shows the correlation between apparent viscosity and temperature.

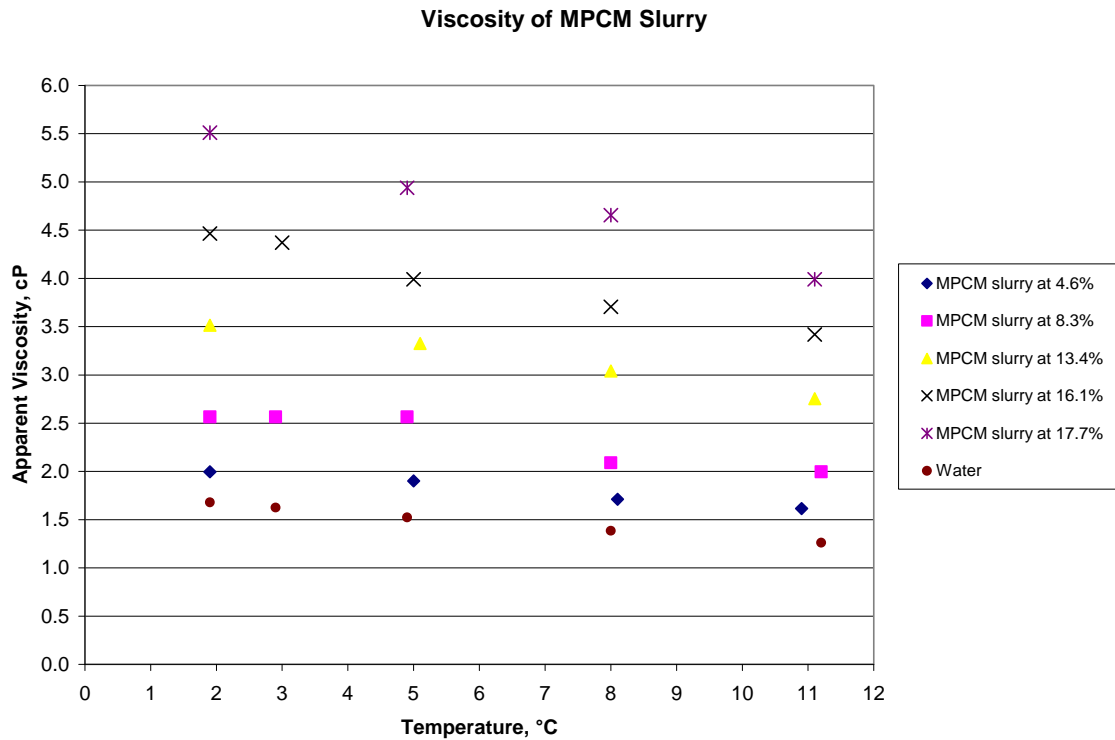


Figure A2. Viscosity of MPCM slurry as a function of temperature.

If one assumes that for each and every value of ϕ , a fluid behaves like a totally different fluid such that the A and B coefficients would differ, then clearly this model would not work, and $A = A(\phi)$ and $B = B(\phi)$. One would need to have some idea of the form of those functions before attempting to fit an equation. It does not seem necessary to make this assumption as long as the values of ϕ are sufficiently small so it still may be assumed that the fluid behaves like water.

If enough data are obtained to explore how this model fits, it would be possible to fit a different temperature-dependency function for several different volume fractions. If different values for A and B are obtained for each volume fraction after the volume fraction effect is removed, then this method may not work well.

If the model is assumed to be in good form, then all the parameters will have to be fit simultaneously to all the data to get the best possible fit. A statistical or mathematics software package may be required, but the equations may be developed and solved independently. It may not even be necessary to use a computational fluid dynamics (CFD) program if a homogeneous fluid is assumed rather than two-phase flow. There is potential for criticism if there is a possibility for doing it simpler. There may be ana-

lytical expressions for this simple problem geometry, recognizing that they may or will be approximations due to turbulence. Nevertheless, these approximate solutions would be as valid as using CFD based on the same approximations in the turbulence modeling.

Viscosity function curve fitting

As a first approximation for understanding the temperature effect, each set of volume fraction data was treated as a separate set of data independent of volume fraction, recognizing the limitation of this assumption as the volume fractions were not constant across each data set. An exponential (with temperature) equation was then fitted to each volume fraction data set. The equation was of the form:

$$\mu = \mu(T) = Ae^{-BT} \quad (\text{A2})$$

where T is the temperature and A and B are constants. The coefficients obtained were very similar and showed a fairly uniform trend from one volume fraction set to another, as shown in Table A1.

Table A1. Coefficients A and B for volume fractions 0 – 20%.

Nominal Volume Fraction (%)	A (cP)	B (1/°C)
0	1.75	0.0270
6	2.67	0.0372
10	4.14	0.0432
12	4.10	0.0351
15	8.70	0.0435
20	9.49	0.0490

Next, using these curve fits, all data were normalized back to a standard temperature in order to isolate the volume fraction effects. The approximate mean temperature of all the tests, 13.75 °C, was selected as the standard temperature.

The first approach to the volume fraction issue was to develop a closed form of the equations for finding the coefficients for the Vand equation given any set of experimental data. That effort produced two very difficult nonlinear simultaneous equations to solve, so a less elegant numerical approach was explored. Using the Solver in Microsoft Excel, the sum of the squares was minimized between the predicted and observed viscosities,

both normalized to 13.75 °C. This minimization, and the resulting fit, was applied across all data. The equation fit was of the Vand form:

$$\mu = \mu(\phi) = (1 - \phi - C\phi^2)^D \quad (\text{A3})$$

where ϕ is the volume fraction and C and D are constants. The initial application yielded $C = 5.26$ and $D = -3.55$, where the volume fraction is dimensionless and the viscosity is in centipoises (cP). Later in the analysis, while looking at the source of the outliers, it was discovered that the most extreme values were from the 20% volume fraction data set, so that data set was eliminated completely and a separate analysis was conducted without it. This second analysis yielded much different coefficients: $C = 12.9$ and $D = -1.66$, where again the volume fraction is dimensionless and the viscosity is expressed in cP.

Next, the Vand correction for volume concentration was used, and similar to the approach used for temperature, it was normalized to a standard volume fraction of MPCM. The mean volume fraction was selected to serve as the normal value, which was approximately 12.8%. Once that correction was made, a new exponential temperature fit was made; this time to all the data as it was possible to isolate the volume fraction effects. This run yielded a single set of new A and B constants and the following “combined effects” equation:

$$\mu = \mu(\phi, T) = 2.09(1 - \phi - 12.9\phi^2)^{-1.66} e^{-0.0380T} \quad (\text{A4})$$

Figure A3 shows the graph made in the process of executing the fits and concisely illustrates the results.

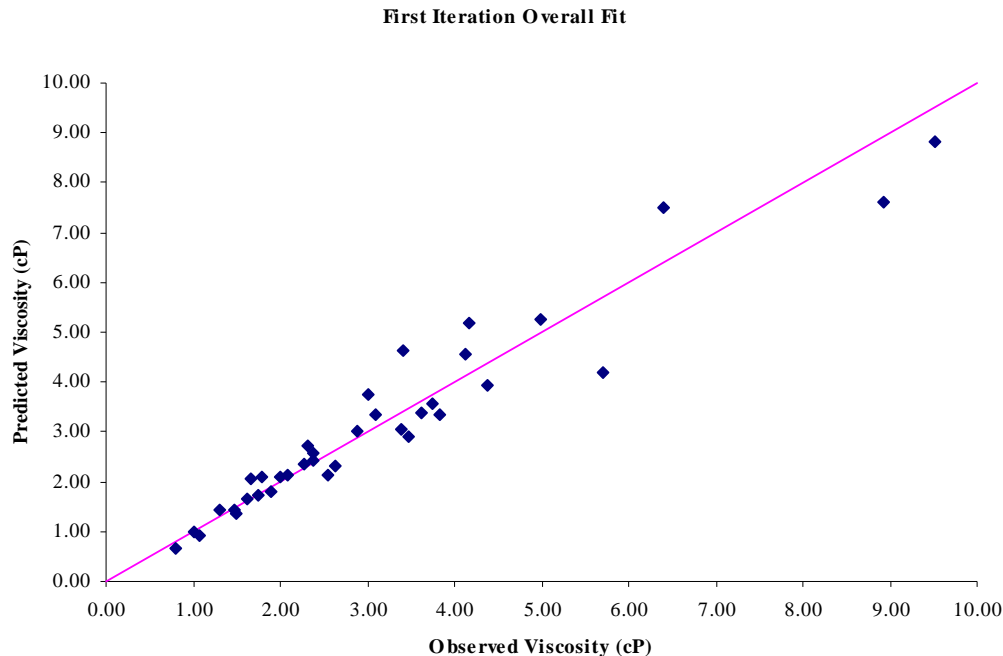


Figure A3. Viscosity curve fitting for first iteration.

The fit appears better at lower viscosities (i.e., lower volume fractions). This result should not be considered conclusive, but it is promising. It is suggested that the analysis be repeated using the kinematic viscosity parameter instead of dynamic viscosity. It is also possible to repeat the fitting process through additional iterations to see if the results improve. The goodness of fit parameter was not computed, but that should obviously be done too. Also, it would be beneficial to repeat the effort after eliminating more of the questionable data. Although it is best to avoid discarding data except for known cause, there was a compelling reason to do so after seeing that all the first-order outliers were coming from the 20% volume fraction data set. Data sets at some of the other volume fractions also were questionable in terms of statistical significance, but unless the data were erroneous, using them should not impact the analysis.

It may be possible to improve the fit while sticking to the overall form of this combined effects equation. Ideally, the fit could be done simultaneously instead of in iterations. However, after developing the basis equations for the Vand-type fit alone, working them out would pose a high level of difficulty at best, and the effort is probably not warranted here. It may be possible to use Excel Solver to do a simultaneous fit, but nonlinear solutions become difficult with many degrees of freedom, and there are no guarantees of a true global minimum when using the numerical routines.

Summary

This analysis provides a useful look at the possible effects of both temperature and volume fraction upon the viscosity of MPCM slurries. The improved viscosity model developed here, while imperfect, will allow for better estimates of required pumping power needs for both retrofitted and new heat transfer piping systems using MPCMs. Using the supplied model, one would be able to find the increase in viscosity of a heat transfer fluid using MPCMs and determine the pumping requirements for their application and piping system, or determine the maximum loading fraction that an existing system can handle.

REPORT DOCUMENTATION PAGE

Form Approved
OMB No. 0704-0188

Public reporting burden for this collection of information is estimated to average 1 hour per response, including the time for reviewing instructions, searching existing data sources, gathering and maintaining the data needed, and completing and reviewing this collection of information. Send comments regarding this burden estimate or any other aspect of this collection of information, including suggestions for reducing this burden to Department of Defense, Washington Headquarters Services, Directorate for Information Operations and Reports (0704-0188), 1215 Jefferson Davis Highway, Suite 1204, Arlington, VA 22202-4302. Respondents should be aware that notwithstanding any other provision of law, no person shall be subject to any penalty for failing to comply with a collection of information if it does not display a currently valid OMB control number. PLEASE DO NOT RETURN YOUR FORM TO THE ABOVE ADDRESS.

1. REPORT DATE (DD-MM-YYYY) 29-03-2008		2. REPORT TYPE Final		3. DATES COVERED (From - To)	
4. TITLE AND SUBTITLE Thermal Performance of Microencapsulated Phase Change Material Slurry				5a. CONTRACT NUMBER	
				5b. GRANT NUMBER	
				5c. PROGRAM ELEMENT	
6. AUTHOR(S) Jorge L. Alvarado, Barclay G. Jones, Charles P. Marsh, David A. Kessler, Chang W. Sohn, Carl A. Feickert, Gary E. Phetteplace, Eric D. Crowley, Ryan J. Franks, and Thomas A. Carlson				5d. PROJECT NUMBER 611102AT23	
				5e. TASK NUMBER	
				5f. WORK UNIT NUMBER 008BE4	
7. PERFORMING ORGANIZATION NAME(S) AND ADDRESS(ES) U.S. Army Engineer Research and Development Center (ERDC) Construction Engineering Research Laboratory (CERL) PO Box 9005, Champaign, IL 61826-9005				8. PERFORMING ORGANIZATION REPORT NUMBER ERDC TR-o8-4	
9. SPONSORING / MONITORING AGENCY NAME(S) AND ADDRESS(ES) Headquarters, U.S. Army Corps of Engineers 441 G Street, NW Washington, DC 20314-1000				10. SPONSOR/MONITOR'S ACRONYM(S)	
				11. SPONSOR/MONITOR'S REPORT NUMBER(S)	
12. DISTRIBUTION / AVAILABILITY STATEMENT Approved for public release; distribution is unlimited.					
13. SUPPLEMENTARY NOTES					
14. ABSTRACT The efficiency of a pumped heat-transfer system can be greatly increased by incorporating a phase-change material (PCM). Because PCMs have greater thermal capacity than the carrier fluid, owing to their latent heat of phase change, they can increase the amount of heat transfer at equivalent volumetric flow in a heat exchanging environment. These materials tend to clog heat-transfer and distribution pipes, but previous research has indicated that the problem may be solved by encapsulating the PCMs. This report documents an investigation of the thermophysical properties of PCMs enclosed in micro-scale capsules. The study also addressed microcapsule durability against abrasion and chemicals, and the relation of fluid temperature and particle volume fraction on viscosity. The results of this research show that the total heat capacity of microencapsulated PCM (MPCM) slurries is enhanced significantly, even when using low volume fractions. MPCM slurries have potential to decrease costs and improve energy efficiency for all pumped cooling applications.					
15. SUBJECT TERMS microencapsulated phase-change materials (MPCM) pumped heat transfer encapsulation tetradecanol viscosity model					
16. SECURITY CLASSIFICATION OF:			17. LIMITATION OF ABSTRACT	18. NUMBER OF PAGES	19a. NAME OF RESPONSIBLE PERSON
a. REPORT Unclassified	b. ABSTRACT Unclassified	c. THIS PAGE Unclassified			SAR